ALMA MATER STUDIORUM
UNIVERSITÀ DI BOLOGNA

DEIS - Department of Electronics, Computer Science, and Systems

Tools and methods for the quality assurance of force platforms in human movement analysis

Thesis submitted for the degree of
Ph.D. in Bioengineering (ING-INF/06)

Student: **Eng. Andrea Cedraro**

Supervisor: **Prof. Angelo Cappello**

Co-supervisor: **Prof. Lorenzo Chiari**

Reviewer: **Prof. Aurelio Cappozzo**

Thesis abstract

The human movement analysis (HMA) aims to measure the abilities of a subject to stand or to walk. In the field of HMA, tests are daily performed in research laboratories, hospitals and clinics, aiming to diagnose a disease, distinguish between disease entities, monitor the progress of a treatment and predict the outcome of an intervention [Brand and Crowninshield, 1981, Brand, 1987, Baker, 2006]. To achieve these purposes, clinicians and researchers use measurement devices, like force platforms, stereophotogrammetric systems, accelerometers, baropodometric insoles, etc.

This thesis focus on the force platform (FP) and in particular on the quality assessment of the FP data. The principal objective of our work was the design and the experimental validation of a portable system for the *in situ* calibration of FPs.

The thesis is structured as follows:

Chapter 1. Description of the physical principles used for the functioning of a FP: how these principles are used to create force transducers, such as strain gauges and piezoelectrics transducers. Then, description of the two category of FPs, three- and six-component, the signals acquisition (hardware structure), and the signals calibration. Finally, a brief description of the use of FPs in HMA, for balance or gait analysis.

Chapter 2. Description of the inverse dynamics, the most common method used in the field of HMA. This method uses the signals measured by a FP to estimate kinetic quantities, such as joint forces and moments. The measures of these variables can not be taken directly, unless very invasive techniques; consequently these variables can only be estimated using indirect techniques, as the inverse dynamics. Finally, a brief description of the sources of error, present in the gait analysis.

Chapter 3. State of the art in the FP calibration. The selected literature is divided in sections, each section describes: systems for the periodic control of the FP accuracy; systems for the error reduction in the FP signals; systems and procedures for the construction of a FP. In particular is detailed described a calibration system designed by our group, based on the theoretical method proposed by Cappello et al. [2004]. This system was the "starting point" for the new system presented in this thesis.

Chapter 4. Description of the new system, divided in its parts: 1) the algorithm; 2) the device; and 3) the calibration procedure, for the correct performing of the calibration process. The algorithm characteristics were optimized by a simulation approach, the results are here presented. In addiction, the different versions of the device are described.

Chapter 5. Experimental validation of the new system, achieved by testing it on 4 commercial FPs. The effectiveness of the calibration was verified by measuring, before and after calibration, the accuracy of the FPs in measuring the center of pressure of an applied force. The new system can estimate local and global calibration matrices; by local and global calibration matrices, the non–linearity of the FPs was quantified and locally compensated. Further, a non–linear calibration is proposed. This calibration compensates the non–linear effect in the FP functioning, due to the bending of its upper plate. The experimental results are presented.

Chapter 6. Influence of the FP calibration on the estimation of kinetic quantities, with the inverse dynamics approach.

Chapter 7. The conclusions of this thesis are presented: need of a calibration of FPs and consequential enhancement in the kinetic data quality.

Appendix: Calibration of the LC used in the presented system. Different calibration set–up of a 3D force transducer are presented, and is proposed the optimal set–up, with particular attention to the compensation of non–linearities. The optimal set–up is verified by experimental results.

Contents

Chapter 1

Force platforms

1.1   Principles of functioning

A force platform (FP) is a complex force transducer.

The functioning of a force transducer is based on different physics principles, like the Ohm's law or the piezoelectric effect: by the appropriate use of these principles, the force exerted on the transducer is converted into a voltage signals (transduction property).

The **Ohm's law** describes the property of conductive materials, such as metals or metal alloys, to allow the passage through the material of a current flow. It can be computed as:

$$R = \frac{l}{A}\rho \qquad (1.1)$$

where:

R is the electrical resistance of the material, measured in Ω;
l is the length of the conductor, measured in meters;
A is the cross-sectional area, measured in square meters;
ρ is the electrical resistivity of the material, measured in Ω·meter.

This law is valid when the current density is totally uniform in the conductor, of regular cross section. In practice, almost in any real conductor the current density is not totally uniform. However, the Ohm's law still provides a good approximation for long thin conductors such as wires. It is worth noting that the resistance is a function of the geometry of the conductor.

The transduction property is obtained by considering the Ohm's law together with the **elasticity property**, present in any solid material. The elasticity can be quantified by the Young's modulus, that describes the relationship between the force applied to a solid body and the solid body deformation:

$$E = \frac{\sigma}{\epsilon} \qquad (1.2)$$

where:

E is the Young's modulus, measured in Pascal;
σ is the applied stress, measured in Pascal;
ϵ is the strain of the material, pure number, usually in microepsilon.

The Young's modulus quantifies the transduction of a force into a geometrical deformation (strain).

Another aspect that must be considered, for the definition of the transduction property is the **Poisson's modulus**. When a force is applied to a rigid body along one direction (longitudinal), the body lengthen/shorten along this direction, but shorten/lengthen along the orthogonal directions. The deformation along the orthogonal directions is opposite to the deformation along the longitudinal direction, since the volume of the body does not change (principle of the volume invariability). This effect is quantified by the Poisson's modulus:

$$\nu = -\frac{\epsilon_t}{\epsilon_l} \tag{1.3}$$

where:

ν is the Poisson's modulus, pure number;
ϵ_t is the strain along a transversal direction;
ϵ_l is the strain along the longitudinal direction.

The transduction property, as perviously described, is utilized by the **strain gauge** (or estensimeter) exemplary shown in figure 1.1.
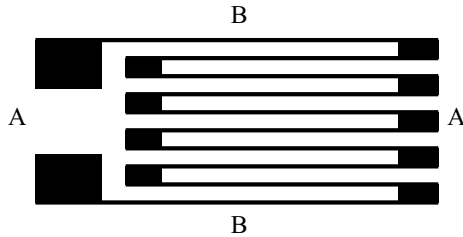
Figure 1.1: Strain gauge representation.

A strain gauge can be made of different materials, such as Constantana or Isoelastic alloys. The particular geometry of the strain gauge (thin and thick wires) makes its resistance mainly dependent on deformations along the longitudinal direction (A).

The thin wires of strain gauge have a resistance much higher than the thick wires, in fact the ratio $\frac{l}{A}$ is $\gg 1$ for the thin, and is $\ll 1$ for the thick wires.

As a consequence, the total resistance of the strain gauge is almost determined by the sum of the thin wires resistances.

Considering a longitudinal deformation ϵ_l, the Ohm's equation 1.1 can be expressed as:

$$R(\epsilon_l) = \frac{l(\epsilon_l)}{A(\epsilon_l)}\rho(\epsilon_l) \tag{1.4}$$

where the quantities function of ϵ_l can be described as their value at rest (l_0, A_0 and ρ_0) and their dependance on the strain:

$$\begin{cases} l(\epsilon) = l_0(1 + \epsilon_l) \\ A(\epsilon) = A_0(1 - \nu\epsilon_l)^2 \\ \rho(\epsilon) = \rho_0(1 + \beta_\rho\epsilon_l) \end{cases} \tag{1.5}$$

The electrical resistivity is also strain dependant, as expressed by the coefficient β_ρ. Expressing equation 1.1 by logarithm and calculating the derivation $\frac{\Delta \log(R)}{\Delta\epsilon_l}$, equation 1.4 can be expressed as:

$$\frac{\Delta R}{R} = \left[1 + 2\nu + 2\beta_\rho\right]\epsilon_l = S_l\epsilon_l \tag{1.6}$$

where S_l is the longitudinal sensitivity of the estensimeter, that represents the transduction between a longitudinal strain and change of electrical resistance.

Anyway, a transversal deformation ϵ_t causes a change of the strain gauge resistance, this change is called **cross–sensitivity** S_t. Since the strain gauge is supposed to measure only strains along the longitudinal direction, a transversal strain, due to the cross–sensitivity, results interpreted as an apparent longitudinal strain. Therefore, the cross–sensitivity can be considered as an undesired effect that must be taken into account and, as far as possible, compensated. Usually, the cross–sensitivity is measured and compensated during the calibration of the estensimeter. Finally the transduction from strain to resistance–change is expressed as:

$$\frac{\Delta R}{R} = S_l(1 - \nu\frac{S_t}{S_l})\epsilon_l = K\epsilon_l \tag{1.7}$$

where K is the gauge (or gage) factor.

The **piezoelectric effect** is the property of some materials, such as quartz or some ceramics, to acquire a charge when compressed, twisted or distorted. This property provides the transduction between mechanical phenomena and electricity. The most used material for piezoelectric transducers is quartz, since it demonstrated to be extremely stable and easy to be shaped. Another characteristic of quartz is that the material is sensitive to the applied mechanical stress along the direction of its crystal lattice. As a consequence, the quartz can be shaped in slices that are selectively sensitive to a particular direction of the applied force: longitudinal, transversal or shear. The **cross–sensitivity** is also present in piezoelectric transducers, and is due to imperfection in the crystal lattice, in the quartz cut; the cross–sensitivity is due also to the volume–invariability effect.

The **electrical output signal**, generated by strain gauge or piezoelectric transducers, is usually measured by the composition of more transducers combined together.

Considering the piezoelectrics, more **slices** are mounted together and each slice is sensitive to a particular direction of the load. For example, two slices sensitive to a shear force, mounted so that their crystal lattice are orthogonal, form a transducer sensitive to both the horizontal components of the applied force; an useful consequence is that the applied force results to be measured in an orthogonal reference frame.

Considering the strain gauges, 4 units are mounted in the **Wheatstone bridge** circuit (figure 1.2). By this circuit, the output of the single transducer result amplified and undesired effects, due for example to the temperature change or to the cross-sensitivity, can be partially compensated.

The bridge can be described as the parallel of 2 voltage dividers. If the transducers on the opposite sides (1–3 and 2–4) undergo to opposite deformations, their resistance will change of a $\Delta R = \Delta R_1 = \Delta R_2 = -\Delta R_3 = -\Delta R_4$ opposite in sign and the voltage output V_u results proportional to ΔR :

$$V_u = V_A \cdot \frac{\Delta R}{R} \tag{1.8}$$

Depending on the used technology, FPs can be divided into piezoelectric or estensimetric. Usually a FP is formed by a metal basement connected to a metal plate (the working layer) by at least 3 supports: in piezoelectric FPs, each support can be formed by more slices of crystal.

In estensimetric FPs, each support can be instrumented with one or more

Wheatstone bridges, glued to its surface. Depending on the orientation of the transducers, the bridges can be mainly sensitive to a compression/traction, shear or torque force, as shown in figure 1.3.Usually, more than 4 transducers are glued to one support and can be combined in more than one Wheatstone bridge: in this way, by a support, more components of the applied force can be measured. Another advantage of having more bridges (or more crystal slices) on the same support is the possibility to compensate non–linear effects due to the non–linearity and cross–sensitivity of the transducers.
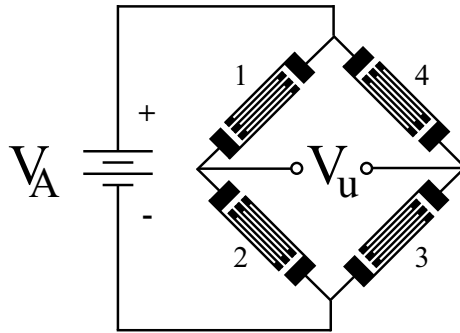
Figure 1.2: Four strain–gauge transducers arranged in a Wheatstone bridge configuration. The bridge is formed by two voltage dividers (1,2) and (3,4). The power supply of the bridge is the voltage V_A while V_U is the bridge output.
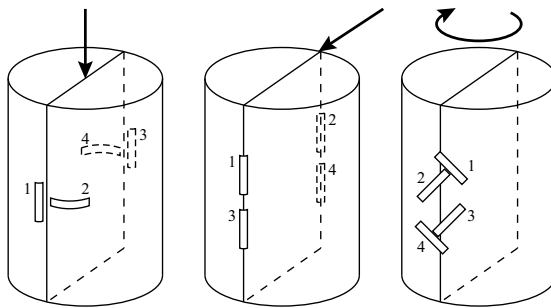
Figure 1.3: Typical Wheatstone configurations. The configurations measure respectively, from left side, traction/compression, shear and torque. It is worth noting that the transducers placed on opposite sides of the bridge (1,3) and (2,4) undergo to similar geometrical deformation, while the transducers placed side by side undergo to opposite deformation.

1.2   Typologies

Force platforms can be subdivided in two classes, depending on the dimension
of their output vector:

- three component;

- six component.

1.2.1   Three component

Three component force platforms measures:

- the vertical component of the force applied to the FP (F_Z);

- the X and Y coordinates of the point of application of the force (x_p; y_p).

These FPs are composed by at least 3 supports that measure the vertical compo-
nent of the applied force. The point of application of the force, usually defined
as the **center of pressure** (COP), is calculated by the moment equilibrium, as
exemplary shown in figure 1.4 and in equation 1.9, for a FP with 3 supports.
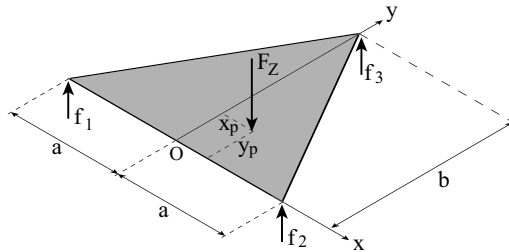
Figure 1.4: Three component force platform, made of 3 supports that measure the
vertical component of the applied force (F_Z). By the moment equilibrium, the point
of application of the force (x_p and y_p) can be calculated.

$$\begin{cases} F_z = f_1 + f_2 + f_3 \\ x_p = \dfrac{f_2 - f_1}{f_1 + f_2 + f_3} \cdot a \\ y_p = \dfrac{f_3}{f_1 + f_2 + f_3} \cdot b \end{cases} \qquad (1.9)$$

1.2.2   Six component

Six component force platforms measures:

- the X, Y and Z components of the force applied to the FP (F_X; F_Y;F_Z);

- the X, Y and Z components of the moment of the force, referred to the origin of the FP reference frame (M_X; M_Y;M_Z).

equivalently, the output can be expressed in the form:

- the X, Y and Z components of the applied force;

- the X and Y coordinates of the COP (x_p; y_p);

- the free torque along the Z axis (M_T).

where Z is the axis normal to the FP surface and X,Y are the shear axes. These two different output form are equivalent and can be converted to the other by equation 1.10:

$$\begin{cases} M_X = F_Z \cdot y_p \\ M_Y = -F_Z \cdot x_p \\ M_Z = F_Y \cdot x_p - F_X \cdot y_p + M_T \end{cases} \qquad (1.10)$$

Usually six component FPs have a rectangular shape and are composed by 4 supports, located in the 4 corners. Each support measures or the 3 components of the force, or both the 3 components of the force and the moment.

From the mechanics theory, all the forces applied to a body can be equivalently expressed by a 3D force, applied to a point on the body surface (COP), and a 3D torque (the resultant force and torque). Since a FP is generally placed on the ground, and loaded by applying forces on its upper surface, the only torque that can be applied to the FP is the torque along the axis normal to the FP surface, that is usually generated, in HMA, by the twist of the foot.

Moreover, the COP of the resultant force must lay on the FP upper surface, as a consequence, the Z coordinates of the COP is fixed and known.

Hence, the interaction, between a FP laying on the ground and an external body, can be described by a 3D force, a torque along the Z axis, and the X and Y coordinates of the COP. In conclusion, the interaction between a body and the FP can be completely measured by a six component FP; by a three component FP, only a part of the interaction can be measured, since the horizontal components of the force and the free torque are not measured.

A sufficient condition to calculate the six component output of a FP is the measurement of the 3D components of the force, in all the supports. Figure 1.5 and equation 1.11, show how to calculate: the moments with respect to the FP center, the X and Y COP coordinates, and the free torque M_T.
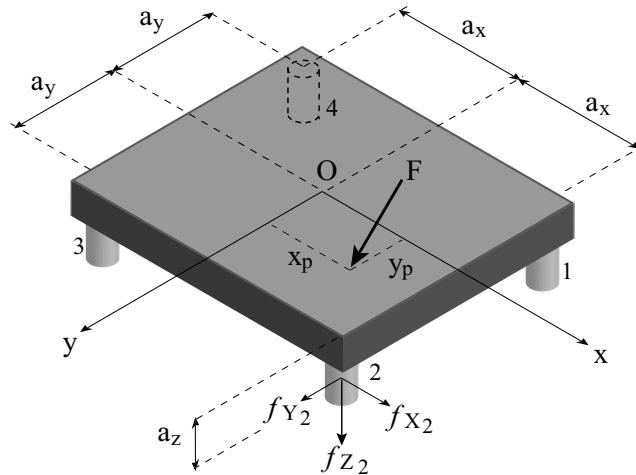
Figure 1.5: Six component force platform, made of 4 supports that measure the X,Y and Z components of the applied force F. The quantities a_x, a_y and a_z, are the distance of the FP axes origin (O), from the origin of the coordinates of the four load cells.

$$\begin{cases} F_X = \sum_{k=1}^{4} f_{Xk} \\[2mm] F_Y = \sum_{k=1}^{4} f_{Yk} \\[2mm] F_Z = \sum_{k=1}^{4} f_{Zk} \\[2mm] M_X{}' = a_y \cdot (f_{Z1} + f_{Z2} - f_{Z3} - f_{Z4}) \\[2mm] M_Y{}' = a_x \cdot (-f_{Z1} + f_{Z2} + f_{Z3} - f_{Z4}) \\[2mm] M_Z = a_y \cdot (-f_{X1} - f_{X2} + f_{X3} + f_{X4}) + \\[1mm] \quad\quad + a_x \cdot (f_{Y1} + f_{Y4} - f_{Y2} - f_{Y3}) \end{cases} \tag{1.11}$$

where F_X, F_Y and F_Z are the 3D components of the force F; f_{Xk}, f_{Yk} and f_{Zk} ($k = 1 \dots 4$) the 3D components of the force measured by the four supports. The quantities $M_X{}'$ and $M_Y{}'$ are the moments referred to the plane parallel to the x, y plane, but crossing the origin of the coordinates of the load cell ($z = a_z$), hence **not** referred to the working plane ($z = 0$). Since the value a_z is known, the COP coordinates can be calculated by equation 1.12.

$$\begin{cases} x_p = \dfrac{F_X \cdot a_z - M_Y{}'}{F_Z} \\[4mm] y_p = \dfrac{F_Y \cdot a_z + M_X{}'}{F_Z} \end{cases} \tag{1.12}$$

The moments M_X and M_X, referred to the origin of the FP reference frame can be calculated by equation 1.12 and 1.10.

As shown in equations 1.11 and 1.12, the output of a six component FP can be calculated only by measuring the force applied to each of the FP supports, and express it in the xyz reference frame. Anyway, this theoretical approach stands on an assumption: the top plate of the FP is considered as an **infinitely rigid body**. This assumption is only approximately true, in fact the upper plate of a FP inevitably goes under deformation, when loaded.

A flexion of the top plate causes a flexion of the supports, and this flexion can be described as a moment applied to the supports. For this reason, by neglecting the moments measurement, errors in the FP output vector will be introduced. The flexion of the top FP plates depends mainly on the extent and COP of the vertical force: a vertical force with a high extent will cause a higher top plate flexion than a force with lower extent, if both applied in the same COP; on the other side, a vertical force applied in the FP baricenter will cause a higher flexion than the same force applied near a support. Theoretically, shear forces contribute to the error in the FP output vector because they induce deformations that can lead to additional moments in the supports. Anyway, the contribute of shear forces can be neglected [Schmiedmayer and Kastner, 2000].

In conclusion the flexion of the FP top plate is mainly due to the vertical force together with the COP coordinates, hence the flexion can be considered as proportional to the moment of the vertical force, referred the FP baricenter (thus the moments about the horizontal axes). A FP with supports that measures only the 3D force are subject to this effect; a possible compensation can be achieved by supports that measure both 3D force and 3D moment [Schmiedmayer and Kastner, 2000]. Anyway, since non–linearities in the mechanical structure of both FP and supports, and in the transduction are always present [Mita et al., 1993], the use of supports made of six component transducers can only reduce and not eliminate the non–linearity effect caused by the flexion of the FP top plate.

1.3   Electrical and electronic hardware

Piezoelectric transducers generate a charge, when mechanically loaded, anyway, this charge has a very small amplitude and a very short time of maintenance. As a consequence, piezoelectrics requires electrical instrumentation for the correct acquisition.

An element present in all of the piezoelectric FPs is a charge pre-amplification; the pre-amplifier increases the amplitude of the electrical signal and increases as well the signal/noise ratio, further, the pre-amplifier reduces the noise due to the connection of the piezoelectrics to other electrical instruments (interconnection error). This pre-amplifier should be the closest as possible to the transducers in order to increase the soon as possible the signal protection to external noise; as an example, even shielded cables can couple with electromagnetic sources in the surrounding (like the home voltage–supply) and introduce errors in the

measured signals.

Piezoelectric transducers can be described by an under-damped second order system, hence low-pass filtering is often used to diminish oscillations. As a consequence, hardware for the signal conditioning and filtering is usually present.

An estensimetric FP requires first of all a voltage supplier, since a Wheatstone bridge works only if a voltage supply is present (V_A in figure 1.2). This supply must be a direct voltage, the most stable as possible, since the output of the bridge is proportional to it. Usually, the output of a bridge is small in amplitude (about 10^{-3} Volts) hence the output requires an amplification, in order to increase the signal/noise ratio and diminish the interconnection error.

The FP output is composed by analog signals, anyway, since FPs are used together with electronic systems (like computers), the data must be converted to digital; to this aim, acquisition devices are used. An acquisition device convert the analog signal into digital and, by appropriate protocols (or drivers), communicate with a computer. Once in a computer, the voltage signal can be recorded and elaborated.

In conclusion, the FP functioning can be summarized as follows:

- a force is applied to the working layer of the FP;

- the force is mechanically transmitted to the supports;

- the supports undergo to a geometrical deformation;

- the deformation is transduced by the sensors into electrical signals;

- the signals are conditioned by electrical, and acquired by electronic instrumentation;

- the electrical signals are converted into force signals by the calibration.

1.4   Calibration

A calibration process aims to give a physical interpretation to the electrical signals coming from a measurement instrument.

To this aim, the measurement instrument is loaded using known inputs "y" (for example forces, temperatures, distances, ...) and the instrument outputs "x" are recorded: calibration is achieved by calculating, with a mean-square approach, the parameter "C" that fits to the expression:

$$y = C \cdot x \qquad (1.13)$$

By the calculated parameter, any electrical output x_i can be interpreted as a physical input y_i.

As a simple example of calibration, a load cell is loaded by known loads α_1 and α_2 expressed in Newton; the load cell measures respectively β_1 and β_2 expressed in Volt. Calibration can be achieved by calculating the straight line that cross the points of coordinates (β_1, α_1) and (β_2, α_2).

The above description is valid only for instruments with one, linear, output signal. If an input–output relationship is non–linear, it can be better described by a polynomial with an order higher than one, for example by using a parabolic or a cubic expression.

For an instrument with more than one output signal (N, for example), a relationship as 1.13 must be estimated for each component of the output vector. This would be the case if the input and output are **linearly proportional**:

$$\begin{cases} y_1 = C_1 \cdot x_1 \\ \quad \vdots \\ y_N = C_N \cdot x_N \end{cases} \qquad (1.14)$$

For an actual measurement instrument, equation 1.14 is only approximately true, since secondary effects, as crosstalk and non–linearity, are always present. For example, with a **linear crosstalk** between the variables, each component of the output vector results proportional to all the elements of the input vector. Calibration can be achieved by estimating the proportional coefficients C_i, where each $C_i = \begin{bmatrix} C_1 & \cdots & C_N \end{bmatrix}$ is a $(1 \times N)$ vector.

$$y_i = C_i \begin{bmatrix} x_1 \\ \cdots \\ x_N \end{bmatrix} \qquad (1.15)$$

For each output element y_i, the element C_i is the proportional coefficient between x_i and y_i, while the other elements of C are the crosstalk of the other

input elements on y_i.

A FP is usually described with a linear relationship and a linear compensation of the crosstalk. Considering the FP output as expressed by forces and moments, the voltage output can be converted by using the following matricial expression:

$$
\begin{bmatrix} F_X \\ F_Y \\ F_Z \\ M_X \\ M_Y \\ M_Z \end{bmatrix} = \begin{bmatrix} C_{11} & C_{12} & \dots & C_{16} \\ C_{21} & C_{22} & \dots & C_{26} \\ \vdots & \vdots & \ddots & \vdots \\ C_{61} & C_{62} & \dots & C_{66} \end{bmatrix} \cdot \begin{bmatrix} V_1 \\ V_2 \\ V_3 \\ V_4 \\ V_5 \\ V_6 \end{bmatrix}
\tag{1.16}
$$

where the elements C_{ii}, $i = 1, \dots 6$ (main diagonal) are the proportional coefficients and the other elements (off-diagonal) are the crosstalk between the variables. The FP output expressed in the form $\begin{bmatrix} F_X & F_Y & F_X & x_p & y_p & M_T \end{bmatrix}$ can be converted in $\begin{bmatrix} F_X & F_Y & F_X & M_X & M_Y & M_Z \end{bmatrix}$ by equation 1.10, then can be calibrated and finally converted back to the previous formalism always by equation 1.10.

Equation 1.16 is the most common method to calibrate FPs, used also by commercial brands (*e.g.* Bertec). Anyway, non–linear effects can always be present and consequently the accuracy obtained with a linear calibration can be not optimal. As described in page 15, the non–linear effect reported in literature is mainly caused by the flexion of the FP top plate. This flexion can be considered as caused mainly by the moment of the vertical force, that can be decomposed into M_X and M_Y moments. In order to take into account this non–linear effect in the calibration process, a **non–linear** calibration, $[\ ]_C$, of the FP output vector can be done by the following equation:

$$
\begin{bmatrix} F_X \\ F_Y \\ F_Z \\ M_X \\ M_Y \\ M_Z \end{bmatrix}_C = \mathbf{C} \begin{bmatrix} V_1 \\ V_2 \\ V_3 \\ V_4 \\ V_5 \\ V_6 \end{bmatrix} + \mathbf{C}_X \begin{bmatrix} V_1 \\ V_2 \\ V_3 \\ V_4 \\ V_5 \\ V_6 \end{bmatrix} M_X + \mathbf{C}_Y \begin{bmatrix} V_1 \\ V_2 \\ V_3 \\ V_4 \\ V_5 \\ V_6 \end{bmatrix} M_Y
\tag{1.17}
$$

where $\mathbf{C}$, $\mathbf{C}_X$ and $\mathbf{C}_Y$ are (6×6) matrices as defined in 1.16.

1.5   Applications in research centers and clinics

The ability of standing and walking (motor ability), without the risk of falling or self–injuring, is a primary need for any human being. A double interest can be found in the study of the motor ability: how does this ability works? and how can be solved or diminished problems related to this ability?
The first question comes from the innate curiosity of human beings, in finding the mechanisms of how nature works; the second question comes from the human empathy [Stazio, 200 B.C.], that turns into social aspects, like the progress in health care.

A lack or an inefficiency in the motor ability can cause loss of equilibrium, falls, and these effects reflects in a diminished life quality: a person with such problems feels less safe and secure and has fear of falling. A consequence of this unsafe state of mind is the reduction of the daily activities and self–independency, in both social and domestic environments; this reduction reflects in an increasing isolation and in a reduced life quality.

The motor ability is the result of a sub-conscious activity of the central nervous system, that collects and elaborates information coming from the surrounding world [Peterka and Black, 1990]. The information comes from the senses of vision and proprioception, and from the vestibular apparatus. By the elaboration of these inputs (sensory integration) the central nervous system tries to find the good activation and coordination of the muscles to perform a motion act, like standing, walking or jumping.

Problems related to the motor ability can be caused by problems in the muscle–skeletal system or in the sensory integration. The muscle–skeletal system can be considered as the "hardware" structure of the human being: bones and muscles sustain and activate the body. Injuries, like bone or ligaments rupture, surgical operations, prosthesis and orthosis implantation, can cause a temporary or a permanent modification of the natural body structure: inefficiency or inability can be caused by the incoming of one of these events. Further, another cause of motor problems can be due to the muscles aging or the muscle diseases: the muscles become less reactive or less effective.
Sensory integration and coordination are activities concentrated in the central nervous system (brain and cerebellum), these elements are responsible of the good functioning of the human hardware structure: without a proper activation or control any machine would be unable to function. Consequently,

problems that diminish the effectiveness of the sensory integration system and
the readiness and effectiveness of the coordination system, cause the reduction
of the motor ability. Such problems are caused by diseases, like Parkinson's or
diabetes, by cerebral palsy, by vertigo, or by stroke.

The most common studies of the motor ability are the analysis of the equi-
librium and of the gait. The study of the **equilibrium** is usually achieved
by the measurement of the force exerted to the ground by a subject standing
quietly in an upright posture. Devices, like force platforms, that measure the
ground-to-foot force (or ground reaction force, GRF) were firstly presented in
[Cunningham and Brown, 1952]. By the GRF measurement, the equilibrium
and sensory integration mechanisms can be studied by objective measurements.
For example, the role of each input (vision proprioception, vestibular appa-
ratus): by changing one input, and measuring the consequent change in the
equilibrium mechanism, it is possible to quantify the influence of that particu-
lar input in the whole integration system. For example, changing the subject's
visual feedback [Litvinenkova and Hlavacka, 1973, Galeazzi et al., 2006, Poko-
rná, 2006], or by galvanic stimulation of the vestibular apparatus [Hlavacka and
Horak, 2006, Mainenti et al., 2007], or changing the proprioception feedback
[Capicíková et al., 2006, Adamcova and Hlavacka, 2007] by a mechanical stim-
ulation of the leg muscles.

But how a force platform can be useful for the investigation of the equili-
brium mechanism? Force platforms measure the COP, and the analysis of the
characteristics of this signal allow the evaluation of the equilibrium ability. One
of the most common index is the Romberg ratio, calculated as the ratio of the
areas covered by the COP signal, with eyes open or closed; from the ratio, the
weight of vision in the sensory integration process can be quantified: the more
this ratio differs from 1, the more vision is important in the balance control.
Other evaluation indexes, used in clinical and research practise, are:

- average distance of the COP from the mean position [Murray et al., 1975,
  Goldie et al., 1989, Kilburn et al., 1994];

- the total excursion of the COP [Kilburn et al., 1994, Fernie and Holliday,
  1978, Rocchi et al., 2004]);

- the mean instantaneous velocity of the COP [Kilburn et al., 1994, Fernie
  and Holliday, 1978];

- the mean frequency of the COP excursions [Hufschmidt et al., 1980, Lakes
  et al., 1981, Guerts et al., 1993, Lucy and Hayes, 1985];

- root mean square body sway velocity [Diener et al., 1984, Uimonen et al., 1994, Prieto et al., 1996];

- principal sway direction, reflecting the relative weight of the antero/posterior and medio/lateral components of the oscillation Oliveira et al. [1996], Rocchi et al. [2004].

Another common study of the human motor ability is the **gait** analysis, in which a subject is asked to perform a motor act in an instrumented room or pathway, where one or more 6-component force platforms are placed. The most common motor acts are: normal–speed walking [Harris and Smith, 1996], running, walking on inclined surfaces [Kadaba et al., 1990], stairs climbing [Della Croce and Bonato, 2007], change of direction, step initiation [Rocchi et al., 2006], *etc.* The objective of the gait analysis is to estimate the kinematics of the body segments, together with the estimation of the kinetic variables, such as the internal forces that load bones and junctions of the person during the motor act. The method used to estimate the internal forces is known as **inverse dynamics** and will be described in the next chapter; this method requires the measurement of all the xyz components of the GRF, hence requires the presence of a 6 component FP.

The gait analysis is used to study diseases like Parkinson [Rocchi et al., 2006], cerebral palsy [De Luca, 1991, Gage, 1991], stroke [Kim and Janice, 2004], spasticity [Winters et al., 1987]; it is also used to evaluate the progress in a rehabilitation program [Harris and Smith, 1996], or the effectiveness of a surgical operation [Harris and Smith, 1996], or of a drug benefits [Burleigh et al., 1995, Rocchi et al., 2002].

In more recent time, another field of interest involved the use of force platforms: **sport**. Since around athletes and sport championships turn the proudness of a country, and a usually also lot of money, sport has became subject of research in order to understand and optimize sportive motion act. Force platform still can be useful in this field [James et al., 2007]; as an example, the commercial company Bertec developed starting blocks formed by force platforms, for a study of the best starting–time performance.

Chapter 2

Inverse dynamics

Inverse dynamics is a mathematical method commonly used in gait analysis, by which it is possible to estimate quantities such as:

- the body center-of-mass, often obtained from a double integration of the ground reaction force (GRF) [Lenzi et al., 2003];

- energetic quantities, such as work or power [Meichtry et al., 2007];

- joint forces and moments [Cappozzo, 1984, Winter, 1991].

These estimates are used to study the motor ability of a subject, or the progress in a rehabilitation trial, or the effects of a drug (like Levodopa, on parkinsonian subjects). Therefore, inverse dynamics should be as more accurate as possible, since clinical and scientific outcomes are drawn from the estimated quantities.

2.1   Direct and inverse dynamics

A **direct approach** starts from the knowledge of the causes of an event and aims to estimate the effects.

This principle, applied to human motion, means that the event is the motor act, the causes are what generated the motion, hence the muscles action, and the effects are the body motion. In this approach, the measured, input variables is the muscles action and the estimated, output variables are the body motion, kinematic, and interaction with the ground. In gait analysis in fact, the body interacts only with the ground and other interactions as the friction with the air, are neglected. The interaction with the ground can be schematized by the GRF, and the point of application of the force (center of pressure, COP), as described in chapter 1.

An **inverse approach**, works exactly the opposite of the direct approach: the input variables are the body kinematic, the GRF and the COP, and the output variables is the muscles action. This approach is the only approach applicable in practise, since the internal muscle action can not be measured, unless very invasive technologies, while the body kinematic and the GRF can be measured by means of non–invasive technologies.

2.2 Body representation

A body moves utilizing several bones, muscles and ligaments, joined in a very complex system. In order to study the human motion, simplified **models** of the reality must be used. The models must be as simplest as possible, so as to be easily usable and the results easily interpretable; still, the models must described with a sufficient accuracy the motion act under study.

The most common models of the human body represent: the bones with straight segments, with a concentrated mass; the bone junction and ligaments with spherical or pivot joints; and the muscles action with the equivalent force and moment, applied in the joints. Also the interaction with the surrounding is simplified by a model: the only interaction considered it the interaction between the body and the ground, other interactions are neglected.

The simplest model is the **mono-segmental** model, also called "inverse pendulum". In this model, the entire body is represented by the foot, supposed rigidly connected to the ground, the ankle joint, represented as a pivot joint, and the whole body, represented as a straight segment, with the body mass concentrated in the **center of mass** (COM). The COM corresponds to the baricenter of the body, approximately located at the height of the belly.

In gait analysis the body is represented with a **multi-segmental** model [Cappozzo, 1984, Kadaba et al., 1989, Davis et al., 1991] and, with respect to the lower limb, a three-segment model (figure 2.1) is used. The interaction of the leg with the ground is concentrated in the GRF. The foot is represented with a rigid triangular body while leg and thigh are straight lines with the corresponding mass (m_L and m_T) concentrated in the COM. The joints are represented with, pivot joints (knee) or spherical joints (ankle and hip); the interaction between the segments is represented by a 3D force and a 3D moment.

The rest of the body (trunk and head) can be represented with one ore more segments, depending on the chosen complexity of the model.

The choice of the most appropriate model to used depends on the motor task studied: in quiet standing posture, a subject will not bend his joints much, therefore, the mono-segmental model can be adequate anyway, if the subject "sways" too much its body, and bend his joints (like the hip or knee joints), the mono-segmental model become insufficient and a multi-segmental must be used.

Inverse dynamics uses kinetic and kinematic data. The **kinetic data** can be measured by a **force platform** and the **kinematic data** can be measured by a **stereophotogrammetric system**. The stereophotogrammetric system consists of at least 2 cameras that can record the movements of reflective markers. The markers, positioned on the skin of the subject, allow the reconstruction of the motion of the body segments. A commonly used protocol for the **markers positioning** was proposed by Davis et al. [1991]: the markers are placed on the antero-superior iliac spines (ASISs), postero-superior iliac spines (PSIs),lateral and medial epicondyles, tibial tuberosities, lateral and medial malleoli, heels and toes. The hip joint center can be calculated by a regression using the PSIs and ASIs markers, as defined in Shea et al. [1997]. In respect with the sagittal plane, the ankle and knee joint centers can be identified with the malleolus and epicondyle markers, respectively.
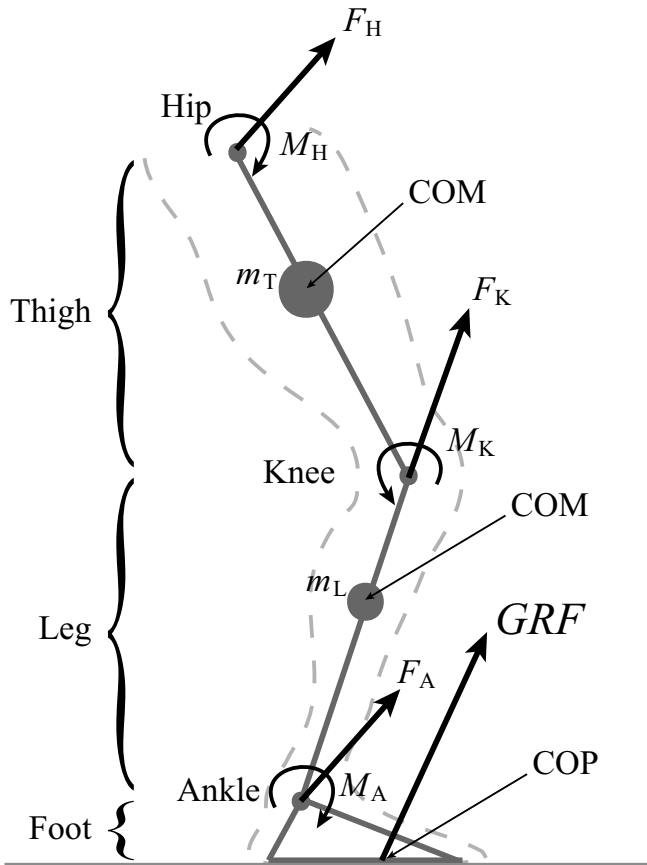
Figure 2.1: Lower limb, in the sagittal plane, represented with a three-segment model. The interaction between body and ground is represented by the resultant force (GRF), applied in the COP. The foot is a rigid triangle, leg and thigh are straight sticks with the respective mass concentrated in the body segment baricenter (COM). The segments are connected by ideal joints and the muscles activity is represented by the resultant force and moment acting in the joint.

2.3 Top–down and bottom–up approaches

In both top–down and bottom–up approaches, each body segment is considered
separately from the other segments and from the external world: the interaction
of the considered segment with the the adjacent segments is described with the
forces and moments interaction (the vincular reaction); the interaction of the
considered segment with the external world is described with the boundary con-
ditions. Each approach starts or with the upper segment (head or trunk–head),
or with the lower segment (foot), ad utilized the boundary conditions (external
forces) to estimates the internal vincular reactions.

The top–down approach starts from the boundary conditions of the upper
segment of the body; this segment has no interaction with the surrounding,
hence the boundary conditions of the free part of the segment (the top of the
head) is that there are no forces and moments applied. Anyway, errors are
always present (section at page 32) and increase while propagating from the
starting segment to the last segment. With a top–down approach, the segment
and joint affected by the largest error are respectively the foot and the ankle.
The ankle is usually the most important joint studied, consequently the ankle
should not have the largest errors. For this reason, the top–down approach is
to be avoided if the subject of interest are the internal forces of the lower joint.

The top–down approach starts from the boundary conditions of the lower
segment of the body, the foot. The boundary conditions of the foot is the GRF.
With this approach, the errors in the foot and ankle are minimized, while the
errors in the upper segment (head or trunk–head) are the largest, for this reason
this approach is the most commonly used in literature, since the objective of
most studies is the estimation of the kinetics of the lower segments.

For each body segment, the mass, the location of the COM and the inertial
parameters can be calculated from anthropometric tabulates [Zatsiorsky et al.,
1990, de Leva, 1996].

The following pages shown how to calculate the joint forces and moments
with a bottom–up approach, using a three–segments model for the lower limb.
The calculation regards the sagittal plane.

The first segment is the foot, equation 2.1 shows how to calculate the ankle forces, horizontal F_{Ah} and vertical F_{Av}, and the moment (M_A), from the horizontal and vertical component of the GRF (F_{0v} and F_{0v} respectively). In the equation, m_F is the whole mass of the foot, concentrated in the COM of the foot, and subjected to the gravity acceleration (g).
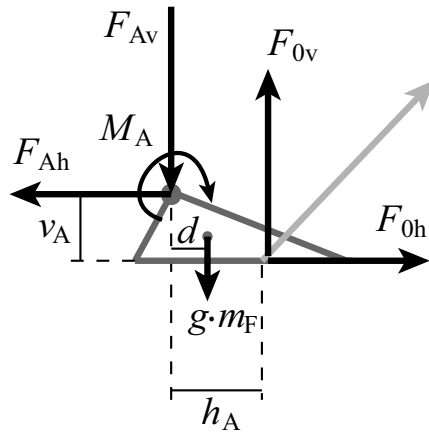
$$\begin{cases} F_{Ah} = F_{0h} \\ F_{Av} = F_{0v} + g \cdot m_F \\ M_A = F_{0h} \cdot v_A + F_{0v} \cdot h_A - g \cdot m_F \cdot d \end{cases} \qquad (2.1)$$

The second segment is the leg, equation 2.2 shows how to calculate the knee forces, horizontal F_{Kh} and vertical F_{Kv}, and the moment (M_K). The foot is substituted with its vincular reactions. The quantity I_L is the moment of inertia of the leg and ϑ_L, $\dot{\vartheta}_L{}^2$ and $\ddot{\vartheta}_L{}^2$ are respectively the angle, angular velocity and acceleration of the ankle. The moment M_L is calculated from the moment equilibrium considering the COM of the leg as pole of reduction.
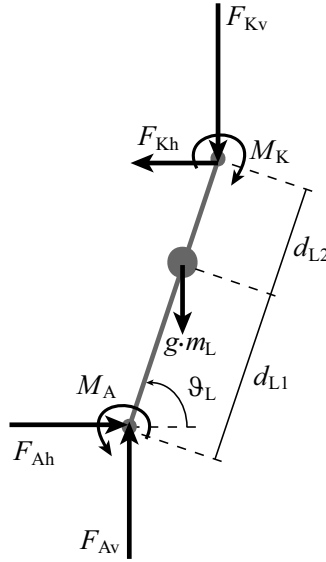
$$\begin{cases} F_{Kh} = -F_{Ah} + m_L \cdot d_{L1} \cdot \left[\sin(\vartheta_L) \cdot \ddot{\vartheta}_L + \cos(\vartheta_L) \cdot \dot{\vartheta}_L{}^2\right] \\ F_{Kv} = -F_{Av} - g \cdot m_L - m_L \cdot d_{L1} \cdot \left[\cos(\vartheta_L) \cdot \ddot{\vartheta}_L - \sin(\vartheta_L) \cdot \dot{\vartheta}_L{}^2\right] \\ M_K = F_{Ah} \cdot d_{L1} \cdot \sin(\vartheta_L) - F_{Av} \cdot d_{L1} \cdot \cos(\vartheta_L) + M_A + \\ \qquad + F_{Kh} \cdot d_{L2} \cdot \sin(\vartheta_L) - F_{Kv} \cdot d_{L2} \cdot \cos(\vartheta_L) - I_L \cdot \ddot{\vartheta}_L \end{cases} \quad (2.2)$$

The third segment of the lower limb is the thigh. In the following, is shown how to calculate the force and moment for the hip joint.
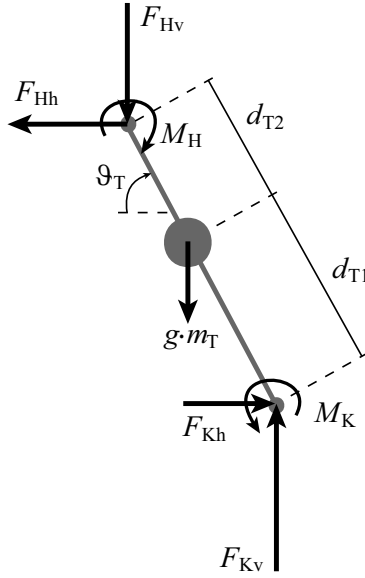
$$\begin{cases} F_{Hh} = -F_{Lh} - m_T \cdot d_{T1} \cdot \left[\sin(\vartheta_T) \cdot \ddot{\vartheta}_T + \cos(\vartheta_L) \cdot \dot{\vartheta}_L^{\,2}\right] \\ F_{Kv} = -F_{Av} - g \cdot m_L - m_L \cdot d_{L1} \cdot \left[\cos(\vartheta_L) \cdot \ddot{\vartheta}_L - \sin(\vartheta_L) \cdot \dot{\vartheta}_L^{\,2}\right] \\ M_H = F_{Kh} \cdot d_{T1} \cdot \sin(\vartheta_T) + F_{Kv} \cdot d_{T1} \cdot \cos(\vartheta_T) + M_K + \\ \qquad + F_{Hh} \cdot d_{T2} \cdot \sin(\vartheta_T) + F_{Kv} \cdot d_{T2} \cdot \cos(\vartheta_T) - I_T \cdot \ddot{\vartheta}_T \end{cases} \quad (2.3)$$

2.4   Sources of error

HMA aims to measure the body kinematic, in particular the absolute and re-
lative movements of the bones, the mechanical transmission of forces between
the bones, and the muscular activity. Since muscles and bones are internal the
body, direct measures can not be applicable unless very invasive techniques, and
indirect measurements must be used. Due to indirect measurements, the bone
and muscles activity is estimated from the measurement of other kinetic and
kinematic quantities, as shown in the previous pages.

In general, every measure is affected by errors, caused by the non–ideality
of the measurement instrument: finite accuracy, influence of the surrounding on
the instrument performance, like the influence of temperature, *etc*. By indirect
measurements, the estimated quantities result more subject to errors, since the
estimated quantities are calculated from measures affected by errors: an error
affecting a measured variable propagates to an estimated quantity.

In the following, the sources of errors, present in gait analysis are briefly
described, and are subdivided into errors related to the kinematics and to the
kinetics.

The most common technique used in literature, for the bone kinematic re-
construction, is the stereophotogrammetry, that consist in the placement of
reflective, or light emitting, markers on the subject skin; the markers movement
is then recorded by two or more cameras and the 3D kinematics of the markers
is reconstructed by an appropriate software. Usually, the markers are placed
following protocols, in which are placed on external anatomical landmarks (or
reperi), like the malleoli or the epicondyles. The kinematics of the markers
therefore, represents the kinematics of the reperi. Further, from the markers
position, the position of internal anatomical landmarks is estimated (like the
hip joint center). The position of the internal landmarks is achieved by regres-
sion techniques, from the position of the markers, as defined in [Crowninshield
et al., 1978, Tylkowski et al., 1982, Andriacchi and Strickland, 1983, Bell et al.,
1989, Davis et al., 1991]. The bones kinematics is calculated by the kinematics
of the internal and external landmarks.

A first source of errors is due to the specific **instrumentation** used: the
finite sensitivity and resolution of the cameras introduces uncertainty in the
measurement of the markers position. Another source of errors is the **mark-
ers positioning**, since the anatomical landmark are manually individuated and

can be affected by errors in the positioning on the skin of the subject [Cappozzo et al., 1996]: these errors affect the location of external landmarks. Further, errors in the markers positioning affect the **internal landmark location**, obtained by regression techniques from the markers position.

The markers are positioned on the skin, during a movement therefore, the markers can move in respect to the bone, since the human body is composed also by soft tissues like the muscles, fat and skin. The movement of the markers in respect to the bones causes an apparent movement of the external and internal landmarks and consequently an error in the estimation of the bones position [Cappozzo et al., 1996, Stagni et al., 2000, Leardini et al., 2005]; this error is known as **soft tissue artifact**. In order to reduce the soft tissue artifact, Cappozzo [1984] proposed an alternative protocol to Davis et al. [1991]: the protocol CAST (Calibrated Anatomical System Technique). In the CAST protocol there are no markers placed on the anatomical landmarks while are used clusters of markers (usually 4 markers per each cluster), positioned on the foots, legs, thighs and pelvis. The position of each anatomical landmark is set in relation to the position of the cluster placed in the same body segment of the anatomical landmark, for example, the epicondyles are set in relation with the cluster positioned on the thigh. The relation in created by a calibration procedure that take place before the gait measurement starts: the landmark is pointed with a stick equipped with markers, the tip of the stick represents the position of the landmark, this position is recorded together with the cluster position. After this procedure, the position of the landmark can be reconstructed from the position and orientation of the cluster. Usually, the landmark is set in relation with the baricenter of the cluster. With this choice, the errors due to the soft tissue artifact is reduced: the cluster baricenter results more insensitive to the soft tissue artifact than a single marker, in fact the markers movement due to the soft tissue artifact is not perfectly synchronous then, opposite movements of the markers compensate each other and the baricenter movement results smaller than the single marker movement. On the contrary, in the Davis protocol, the markers positioned on the anatomical landmark undergo to large errors due to soft tissue artifact, since result positioned in part of the body where the skin movement is higher than in the central part of body segments.

Internal kinetic quantities, like joint moments, forces and power, are estimated by an inverse dynamics approach from external kinetic data such as the GRF, usually measured by a FP.

Over time, the aging of the FP, its usage, and *in situ* installation procedures may change the instrument's sensitivity, and attenuate the crosstalk compensa-

tion ensured by the manufacturer, leading to a lack of accuracy Chockalingam
et al. [2002]. This lack of accuracy introduces **errors in the FP data** and,
consequently, these errors can propagate to the calculated kinetic and ener-
getic quantities. This effect was already reported in literature [Bobbert and
Schamhardt, 1990, Schmiedmayer and Kastner, 1999] and demonstrated to in-
fluence the estimated, internal, kinetic quantities: Mc Caw and De Vita [1995]
showed how an error of ± 5mm or ± 10mm in the COP measurement caused a
variation of the 7% and 14% respectively in the maximum values of the internal
joint moments. Similar results, as the one obtained by Mc Caw and De Vita
[1995], are presented in figure 2.2.

Figure 2.2 clearly shows how an error in the COP measurement influences
the estimation of kinetic quantities such as internal joint moments. Anyway,
this result investigate only partially the effect of errors in the FP data, since
the COP is only one of the variables used in the inverse dynamics; errors in the
other variables, like the GRF, are neglected.

A lack of calibration reflects in errors in all the measured variables, and these
errors can have a greater influence on the estimated kinetic variables. This topic
will be discussed in chapter 6.
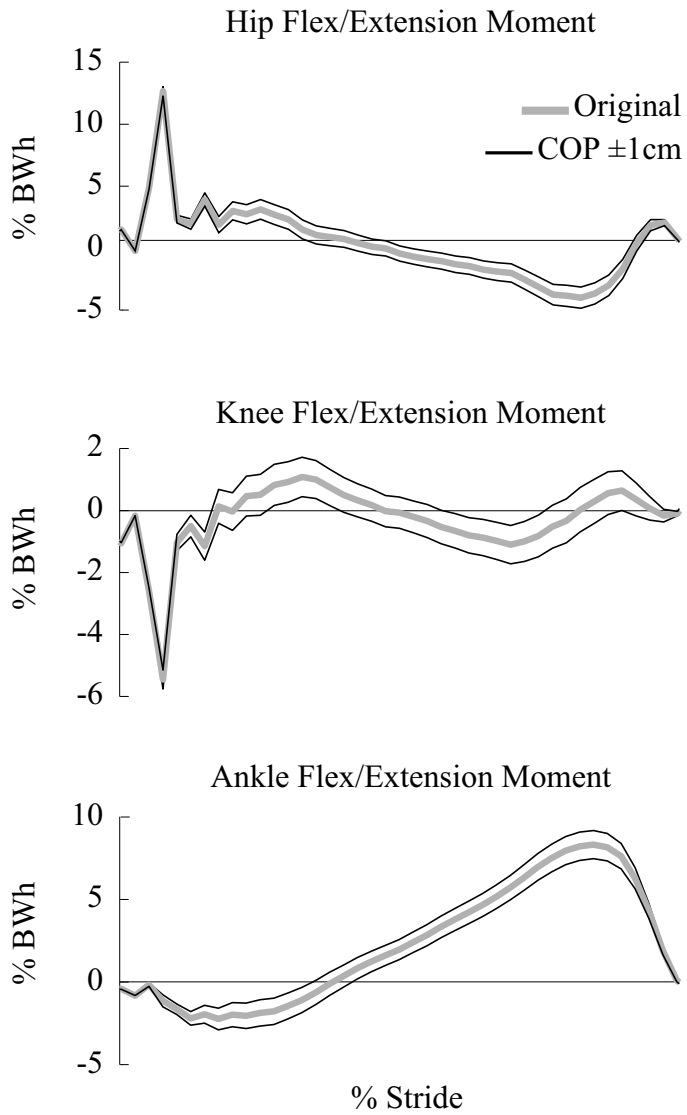
Figure 2.2: Propagation of a COP mislocation (±1cm) on the estimated internal joint–moments. The COP influence on the moments was firstly presented by Mc Caw and De Vita [1995].

Chapter 3

State of the art in the force platform calibration

In this chapter, the state of art in the force platform calibration is described. The presented literature is divided in 4 sections.

The first section describes the techniques that aims to quantify the accuracy of the signals, measured by a FP. A routine control of the FP accuracy is important since it can guarantees the quality of the results obtained from the FP data. Anyway, a control can only "produce evidence of the FP performance and identify failures" [Lewis et al., 2007], hence no intervention on the FP functioning is made.

The second section describes the techniques that aims to optimize (or correct) the accuracy in the COP measurement. The presented papers describe devices and usage–protocols for the data collection and algebraic formulas for the COP correction. These techniques are optimal for posture tests, since in posture tests the most important signal is the COP. Anyway, these techniques are not suitable for the gait analysis, since the variables different from the COP, like shear forces and moments, are not corrected.

The third section briefly describes the methodologies for the construction of a six component FP, or the detailed characterization of the static and dynamic characteristics of a FP. The papers here presented can be considered as an useful instrument addressed to the custom creation of a force platform.

The fourth section describes two papers in which the (6×6) calibration matrix of a FP is estimated. The main advantage in the use of the calibration matrix is that all the six output signals of a FP are corrected: the presented techniques are suitable for both posture and gait tests. One of these two papers ([Cappello et al., 2004]), will be described with more details, since it describes an algorithm that was the starting point for the system subject of this thesis.

3.1   Systems for a quality control

A control of the quality of the FP data can be considered as the first step for any following correction or calibration procedure. Usually, for any measurement instrument, a control of the signal accuracy or the correct functioning of the instrument is performed before the instrument usage. In general, the con-

trol is done by the application of known input signals to the instrument and comparing these inputs to the instrument outputs. The difference between the input and output can be considered as an index of the instrument performance. This difference is compared to a threshold, or a set of thresholds, by which the functioning is discriminated between good or bad, or with a more detailed score values. In case of a positive result, the instrument is considered to function correctly; in case of negative result, the instrument must be calibrated. A control procedure should be performed easily and quickly, since it is only a preliminary activity, before the real usage of the instrument.

In regard of FPs, a simple control procedure is placing known weights on the FP (thus known vertical forces), and comparing the measured vertical forces with the actual weight values. Another simple control procedure can be the application of forces on known COPs on the FP surface, and comparing the measured COPs with the actual COPs.

All the paper presented in the following describes *in situ* techniques, since the techniques can be applied without disassembling or moving the FP under test; an *in situ* technique allows an easier, faster and more economic control of the FP performance.

The first paper, in the author knowledge, about a control procedure for the FP accuracy was published by Bobbert and Schamhardt [1990]. In this paper, calibrated masses, ranging from 0 to 2000 Newton, were applied to a Kistler FP (type 9287). The weights were placed on a wooden board, sustained in one corner by a stylus and the stylus was placed to the FP under test. The positioning of the stylus tip on the FP was facilitated by the use of an aluminium plate, of the same dimensions of the FP and placed on the FP. The plate was designed with 117 holes (COPs), where the stylus tip was located. The FP accuracy was quantified by the difference between the actual COP values and the measured COP values: the paper reported large errors (± 2 cm) arising, as a consequence, the necessity of quality control for FPs, for all the FP users.

Advancement in the technique proposed by Bobbert and Schamhardt [1990] were published by Gill and O'Connor [1997], that proposed a device and a procedure for a faster and more automatic loading of the FP under test. The device proposed by Gill and O'Connor [1997] appeared also in a technical report [CA-MARC II, 1994], and was constructed with two set of orthogonal rigs, mounted with a trolley on top: the trolley could be translated in the x and y directions. On the trolley were placed weights (20, 30 and 40 Kg), part of the weight loaded a steel rod, positioned on an AMTI force platform (type OR6-6-1000). The rod

tip was placed in 121 different COPs. The FP performance were analyzed in the COP accuracy, in the error of the vertical force measurement and in the crosstalk of the vertical force on the shear forces. The errors in the FP measurement resulted to decrease while the load increased (inverse proportionality).

The limitations of this work are the complicated structure of the device, the very high number of measurements and the neglecting of a possible small inclination of the FP. If a FP is not perfectly horizontal, a vertical force would be decomposed, in the FP reference frame, in a vertical and horizontal force, with the horizontal force proportional to the angle; for example, with an angle along the x axis of $\alpha = 0.1°$, with a vertical force of $F_Z = 40Kg = 392N$, the FP will measure $F_X = F_Z \cdot \alpha = 0.7N$, that represent the 0.17% of the vertical force. The result of the example is comparable to the results obtained by Gill and O'Connor [1997]. Moreover the slightly inverse–proportionality of the error with the vertical force is an obvious result, since a measurement instrument result the more precise when the measured variables get closer to the instrument full scale.

The papers previously presented used static, single–point loading. Middleton et al. [1999] used static, distributed loading, by loading the FP with two metal blocks with a rectangular base(25×10 cm). In this paper, the error in the COP measurement resulted the half as was reported by Bobbert and Schamhardt [1990]. The different result was explained by a combination of two effects, the size of the FP and the different load distribution: the FP used by Middleton was shorter than the one used by Bobbert, and the forces applied to the FP were distributed for Middleton and single–point for Bobbert. Both effects were explained as due to the deformation of the FP top plate: in a long FP (as well as with a single–point loading) the FP top–plate undergoes to larger flexion, than in a short FP (or with a distributed, FP loading).

A practical disadvantage of the method proposed by Middleton et al. [1999] is the heavy weight of the metal block, that reflects in an uncomfortable use of the device.

Other authors presented a dynamic, single–point loading system [Baker, 1997, Holden et al., 2003, Lewis et al., 2007]. The idea, firstly proposed by Baker [1997], is the use of a pole by which loading the FP through the pole tip. This technique must be used together with a stereophotogrammetric system, since the orientation and motion of the pole must be measured in order to calculate correctly the force that act on the FP. The pole tip is positioned in 5 COPs of known coordinates. Lewis et al. [2007] instrumented the tip of the

pole with a force transducer (AMTI walker sensor, MCW-250), consequently, the actual COP value and the applied force result both known. The input signal applied to the FP can be calculated by knowing the COP, the kinematics of the pole and the force applied by the pole to the FP. The input signal of the FP results known and the FP output signal can be compared to it.

The use of the pole has a double advantage, the first is the possibility of the application of a 3D dynamic force, instead of a static one, the second is the easy and comfortable use of the device and its high portability. Further, a periodical control of the FP functioning is motivated by the short–lasting duration of the control procedure. Limitations of this idea are the low range of the applicable force (about 135N [Lewis et al., 2007]), and the influence of the stereophotogrammetric accuracy on the input signal calculation.

Fairburn et al. [2000] presented a system that used a dynamic force that simulated the human gait during the sway phase. The system is composed of a pendulum with a lead mass (20Kg) in one extremity, the pendulum is joined to a parallelogram structure, positioned on the FP surface. The free oscillation of the pendulum was recorded by a camera and the FP signals were recorded as well. The pendulum kinematics and kinetics were mathematically reconstructed and the theoretical GRF was calculated. By the comparison between the theoretical and measured GRF, the FP performance were quantified, statically (force–amplitude errors) and dynamically (phase distortion).

3.2 Systems for the COP optimization

An intervention on the FP signals is usually done at the end of the measurement chain. No direct intervention to the hardware structure of the device are done, but only intervention to the measured voltage signals. This approach has a double advantage, firstly it can be easily achieved, without complicated and delicate manipulations of the FP structure, then any intervention on the measured variables is reversible and modifiable. In this approach, the FP signals are considered from the mathematical point of view and the interventions on the signals can be described by mathematical functions.

The first authors, that applied a mathematical approach for the COP optimization, were Bobbert and Schamhardt [1990]. In this paper, the optimization

formulas were polynomial and parametric functions (named as correction algorithm), calculated from the signals acquired by the device and procedure described previously. The parameters of the function were estimated in order to achieve the best fitting between input and output signals.

The polynomial approach was also used by Bing et al. [1996], that developed a stairway connected to two FPs and used a cubic polynomial to compensated the errors measured in the COP signal.

The correction algorithm were further analyzed by Mita et al. [1993], Sommer et al. [1997] and Schmiedmayer and Kastner [1999]: as resulted from those papers, the COP accuracy was enhanced. A limitation of the use of such formulas was reported by Schmiedmayer and Kastner [2000], that stated that in some cases the formulas can overcompensate the error, hence can become itself as a source of error.

Morasso et al. [2004] minimized the COP error by means of a linear transformation, mathematically interpretable as a geometrical isometry of the x and y axis. The data were collected using a device formed by a heavy mass (35Kg) positioned in the center of the FP, and an eccentric mass (2Kg), connected by a rod to the center of the heavy mass. The eccentric mass was set in rotation and the rotation reduced its velocity due to friction: the COP signal generated by the two masses describes a spiral. The geometrical properties of the spiral should be isotropic, hence polar uniformity should be satisfied. From the covariance matrix, calculated from the theoretical and measured spirals, it is possible to estimate the eigenvalues that describe the transformation of one spiral into the other (figure 3.1). By this mathematical operation, the measured spiral result transformed into the theoretical, and the anisotropy in the COP measurement results compensated.

3.3   Custom force platforms

In some cases, it could be useful or necessary the creation of a custom FP, instead of buying a commercial one. In the case, it could be useful to have advices, instructions and methodologies that help in the construction process. Further, after the construction of the FP, its static and dynamic characteristics – such as sensitivity, non–linearity, natural frequency, etc. – must be quantified, and a
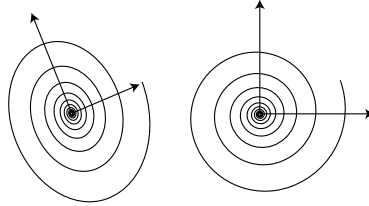
Figure 3.1: COP optimization as presented in Morasso et al. [2004]. The COP trajectory measured by the FP describe an non isotropic spiral (on the left), while the theoretical trajectory is an isotropic spiral (on the right).

paper that deals with these problems could be a helpful instrument.

Browne and O'Hare [2000] presented a procedure for the complete characterization of a FP. This paper give the detailed description of static and dynamic tests for the quantification of the characteristics of a FP such as: linearity, hysteresis, repeatability, natural frequency, non–linearity, signal noise, etc. The paper refers to previous published papers, where the technical characteristics of the transducers are discussed, for example, the offset voltages of each of the transducers should be the same for all of them otherwise the COP measurements will be inaccurate [Beppu et al., 1985, Mita et al., 1993], and the transducers should have a non–linearity $<0.1\%$ full scale [Bizzo et al., 1985]. The procedure described is similar to the procedure usually done by commercial manufacturers or by metrological certification companies, when constructing or certifying a measurement instrument (like a FP); this paper, therefore, could be useful when building a custom FP.

The construction and characterization of a custom six–component FP was published by Gola [Gola, 1980b,a]. The FP described in those papers is a triangular plate, kept in suspension by strips, connected to the plate vertexes and equipped with strain gauges. Each voltage output of the FP (6 signals) was calibrated with second order polynomial functions. This paper could be used also for FP with a structure different from the one used by Gola, since the analytical study of the FP functioning remains valid.

3.4   Systems for the calibration matrix estimation

As described in section1.4 (page 17), the calibration matrix gives a more accurate description of the FP functioning, in respect of the sole optimization of the COP signal. In fact, the matrix is composed by the proportional coefficients (main diagonal elements) and the crosstalks (off-diagonal elements). Each row of the calibration matrix is composed by one of the diagonal elements and by five crosstalk elements. The main diagonal element represent the sensitivity of the FP to a particular component of the load (for example F_X), and the crosstalk elements represent the cross-sensitivity of the other components of the load on F_X. By a (6×6) matrix, all the sensitivities and crosstalks of the FP output vector result quantified.

Hall et al. [1996] developed a system for the estimation of the calibration matrix, using 2D static loads. The loads were applied by means of 2 devices, one for the vertical and one for the horizontal component of the load. The device for the vertical loading of the FP was similar to the device presented in [Gill and O'Connor, 1997]: calibrated weights (up to 1250N) were applied by a stylus in 9 positions on the FP surface. The device for the horizontal loading of the FP was composed by rigs and pulley and allowed the application of calibrated weights ranging ± 500N. The moment components corresponding to each applied load were calculated using the knowledge of the COP and of the force components of the load. As a consequence, the input vector (L_e) of the FP could be calculated. The vector L_e was compared with the measured output vector (L_m) of the FP; the calibration matrix ($\mathbf{C}$) was calculated using a least–squares regression between L_e and L_m:

$$\mathbf{C} = \left(L_m{}^T L_m\right)^{-1} L_m{}^T L_e \qquad (3.1)$$

The matrix $\mathbf{C}$, as previously defined, is a linear operator from forces and moments into forces and moments. Its physical meaning is different from the matrix defined in equation 1.16, in which the linear operator was from voltage signals to forces and moments.

The matrix defined in 3.1 can be decomposed in 4 (3×3) sub-matrices, that dimensionally are pure numbers [1], meters [m], or inverse meters $[m^{-1}]$:

$$\mathbf{C} = \left[\begin{array}{cc} [1] & [m^{-1}] \\ {[m]} & [1] \end{array} \right] \qquad (3.2)$$

By such matrix, the voltage FP output is not needed for the FP calibration process. The FP is considered as a "black box" from which only the force and

moment output vector is given; the calibration process calibrates the signals already expressed into forces and moments.

Assuming a linear model for a six–component FP, the input–output relationship can be arranged as presented in Berme and Cappozzo [1990]:

$$L_C = \mathbf{C} \cdot V \qquad (3.3)$$

where L_C is the calibrated load vector of the FP; $\mathbf{C}$ is the (6×6) calibration matrix, and V is the voltage vector of the FP. Since in most practical cases the acquisition system is a closed box, the voltage signals of the FP are not directly accessible to the user and equation 3.3 cannot be applied. The only outputs available are the load signals already expressed in N and Nm. The model proposed by Berme is still valid, but the calibration matrix $\mathbf{C}$ results dimensionally expressed as defined in equation 3.2:

$$L_C = \mathbf{C} \cdot L_{FP} \qquad (3.4)$$

where L_{FP} is the FP output in N and Nm.

Ideally, if there were no changes in crosstalk and in the sensitivities, $L_C = L_{FP}$ hence the calibration matrix would be the (6×6) identity matrix. The identity matrix can be considered as a meter of comparison for the FP functioning: the more $\mathbf{C}$ results different from the identity matrix, the more the FP was "out of calibration".

The system proposed by Hall et al. [1996] allowed the calculation of the calibration matrix hence allowed the complete calibration of the FP. Anyway, the calibration device resulted heavy and complicated to construct and to use; further, the loads had to be applied precisely along two selected axis of the FP: this requirement made the usage of the device more complicated and the estimation of the calibration matrix more subject to errors due to misalignment in the application of the 2D loads.

3.4.1 System based on Cappello et al. [2004]

Cappello et al. [2004] presented an iterative, weighted–least–squares algorithm that estimated the FP calibration matrix, based on 2D, time–varying loads. The algorithm was developed aiming to the realization of a device and a data–acquisition procedure that responded to the following requirements: easy usage,

high portability and short–time procedure.

The data–acquisition procedure was achieved by applying several load configurations to the FP and recording the output signals of the FP. The calibration matrix $\mathbf{C}$ was estimated by solving equation 3.4 through a least–squares estimation [Draper and Smith, 1966]. To provide independent load configurations, known vertical forces F_V, and known horizontal forces F_H, were simultaneously applied to the FP in known COPs. Each force F_H was approximately oriented along one of the two horizontal axes of the FP reference frame, x or y. The forces F_H and F_V should not be correlated to each other, since with linearly dependent signals the calibration matrix cannot be estimated. Moment components applied to the FP were calculated from the known forces (decomposed along the FP reference frame xyz), and the known COP:

$$\begin{cases} M_X = F_Z \cdot y_{COP} - F_Y \cdot z_{COP} \\ M_Y = -F_Z \cdot x_{COP} + F_X \cdot z_{COP} \\ M_Z = F_Y \cdot x_{COP} - F_X \cdot y_{COP} \end{cases} \qquad (3.5)$$

where x_{COP}, y_{COP}, and z_{COP} were the coordinates of the COP in the FP reference frame. In particular, the absolute value of z_{COP} was the height of the application point of the force from the FP surface, for example when the force was applied to the FP through a rigid body positioned on the FP surface.

The data measured by the FP and by the calibration device were processed in order to estimate $\mathbf{C}$, by a robust algorithm. The algorithm was based on the solution of an iterative, non–linear, weighted, least–squares problem, which accounted for errors in the orientation of the device. These orientation errors (figure 3.2) affected the horizontal force F_H and were due to imperfections in horizontal alignment (an azimuth error essentially due to the manual positioning of the device) and vertical alignment (elevation errors due to, for example, an unlevel floor).

The angles were linearized and were estimated by the algorithm, together with the elements of $\mathbf{C}$.

A design of the device is shown in figure 3.3. The device standed on three supports, two rear feet positioned outside the FP under test, and a steel foot positioned in known COPs on the FP surface. The rear feet were connected to a linear motor (System—Rosati, PE 50/50-B) that moved back and forth, during the measurements for the data–acquisition procedure; the motor was rigidly connected to the upper layer of the device, that resulted translated as
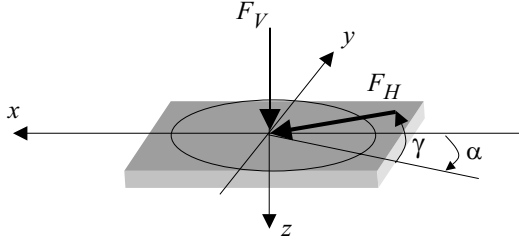
Figure 3.2: Errors (magnified for better visualization) on orientation of calibration force. Elevation γ and azimuth α of horizontal component with respect to force platform reference frame xyz.

well. The motor also acted on a linear spring that transformed the movement into a force; the force was transmitted to a monoaxial load cell (Laumas SA60, FS=600N, accuracy class $< \pm 0.01\%$ FS, repeatability 0.008% FS). The force measured by this load cell was considered as the known input force F_H. This force was transmitted to the upper layer of the device and to the FP, through the steel foot; the part of F_H transmitted to the upper layer introduced an error, since it created a difference between the force measured by the load cell and the force effectively applied to the FP. In order to reduce this error, the upper layer was connected to the other elements of the device by low friction sliders (Star, 1651-814-10). As a consequence of the movement of the upper layer, the part of F_H transmitted to the upper layer reduced to a dynamic friction, that is usually much less than static friction. If dynamic friction is proportional to the translation velocity (viscous friction), as was hypothesize, then by applying a constant velocity to the upper layer, the dynamic friction becomed constant and was eliminated by subtracting the mean values to all the input and output signals:

$$L_C - \overline{L_C} = \mathbf{C} \cdot \left(L_{FP} - \overline{L_{FP}} \right) \tag{3.6}$$

where $\overline{L_C}$ and $\overline{L_{FP}}$ are the mean values of the signals. To achieve a constant velocity of the top plate, a triangular profile was imposed to the linear actuator. Only the portions of the acquired signals that exhibits constant velocity ware retained for data analysis.

The vertical load was generated by a subject standing on the upper layer of the device; the subject created a time–varying force, not correlated to F_H, by

swaying his body. Part of the load generated by the subject was transmitted to another monoaxial load cell (Metior CVF, FS=1000N, accuracy class $\pm 0.1\%$ FS, repeatability $\pm 0.03\%$ FS) and to the FP: this part of the load was considered as the known input force F_V. With a subject standing on the device, the FP resulted loaded in its usual working range (approximately the weight of a person), anyway, the device itself remained lightweight.

The loads resulted applied to the FP through the vertex of the steel foot: the coordinates of the foot vertex were the COP coordinates, in particular, the height of the foot was the absolute value of z_{COP}, as expressed in equation 3.5. No torque should be transmitted to the steel foot, since it would be measured by the FP but not by the load cells: to avoid moment transmission, the coupling between the device and the foot (COP) was designed as a ball and socket junction. The base of the steel foot was designed with a wide area (ϕ=10 cm) to avoid inaccuracies due to FP deformation [Bobbert and Schamhardt, 1990, Middleton et al., 1999, Schmiedmayer and Kastner, 2000] and to simulate approximately a human foot.
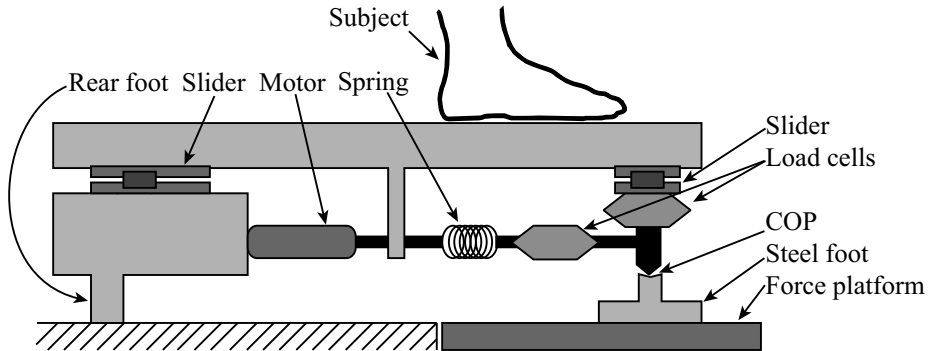
Figure 3.3: Design of the device.

The data–acquisition procedure consisted in the positioning of the device in 5 COPs, and for each COP, the device was oriented along x and y axis, for a total of 10 measurement trials. In each trial, the upper layer of the device was set in movement, and contemporarily the subject swayed his body. Both load cells and FP outputs were recorded by two independent acquisition systems.

Good points of the system based on Cappello et al. [2004].

By this system based on Cappello et al. [2004], the calibration procedure was performed using a time–varying force with a range close to the typical range in which a FP is used in balance or gait analysis: this aspect is important since a calibration matrix results more effective in the range of forces used during the calibration procedure. In fact, since the FP functioning presents also non–linear aspects [Bobbert and Schamhardt, 1990, Schmiedmayer and Kastner, 2000], and a (6×6) calibration matrix is a linear operator: by a linear calibration, the FP non–linearities are linearizes, hence approximates. By a calibration, with signals "centered" on the usual working range, the linearization introduced by the **C** would result optimal for those signals as well.

Another important aspect of the described system is the use of time–varying forces, despite static ones. A time–varying force explore the FP functioning in more points of the xyz volume defined by the force used during the calibration procedure; by a static loading, only few points of this volume would be explored, while a continuous, time–varying force explores much more of this volume.

The forces used, anyway, remained always confined in a plane (xz or yz respectively): the use of a 3D force would increase the exploration of the xyz volume, and this could reflect in a more accurate calibration.

The calibration device 3.3 weighted about 25Kg: this allowed the system to be transportable and usable *in situ* . Anyway, the weight of the device was still too high for a comfortable usage by an user: the data–acquisition procedure required a careful and accurate placement of the device in 5 points, 2 times per point, and all these operations were performed with a high amount of stress for the backbone of the user.

Weak points of the system based on Cappello et al. [2004].

The generation of the 2D force was carried by the linear motor (F_H) and by a subject (F_V). From the theoretical approach, the subject was supposed to generate a pure time–varying vertical force: this can be only an approximation, since it is impossible, for a human subject to move in a plane only, it is sufficient to look to any statokinesigram, for example in [Rocchi et al., 2004], to notice that an upright posture requires a 3D force (vertical and both in the x and y directions) for the balance maintenance. Therefore, inevitably, a force is always

present in the direction normal to the plane defined by F_H and F_V; the load cells used in the device were monoaxial and were positioned to measure F_H and F_V respectively: a force in the normal direction was not measured but in any case resulted transmitted to the FP under test. This effect created differences between the measured, input signals and the input signals actually applied to the FP: this introduced errors in the calibration matrix estimation.

A possible solution of this problem could be using a motor for the vertical movement also; a problem with that solution would be the necessarily heavier weight of the structure and the consequent less usability.

Anyway, even in the hypotheses of such solution, the algorithm should be modified: an unlevel floor or an inclination of the device would reflect in an inclination of the force F_V, the possible inclination of F_V was not considered by the algorithm (figure 3.2), and this may introduce errors in the matrix estimation. Since the load cells ware mounted orthogonally, the elevation angle γ influences both force signals, hence the misalignment angles should be modified as shown in figure 3.4 (A). Anyway, an inclination of the device in the frontal plane, 3.4 (B),would require the introduction of another misalignment angle β, not considered in the published version of the algorithm.

In conclusion, the system here described had the following good points:

- estimation of the calibration matrix;

- use of time–varying forces;

- portability, for the *in situ* calibration;

- short–time calibration procedure;

- non–point loading of the FP.

On the other side, the weakness of this system were:

- use of 2D forces;

- only partial correction of the misalignment angles;

- linearization (hence approximation) of the angles;

- still too heavy device.
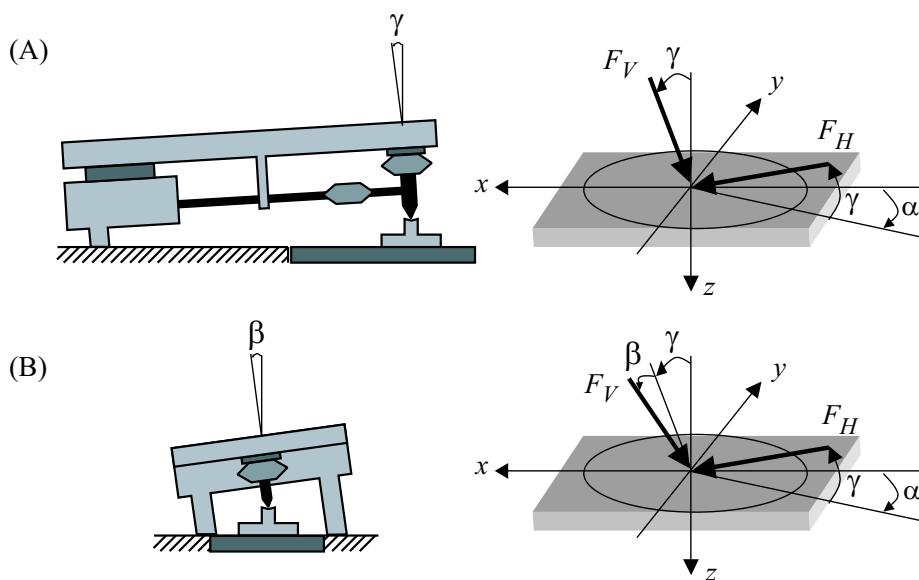
Figure 3.4: (A) An inclination of the device on the sagittal plane, angle γ (magnified), influence both F_H and F_V forces. (B) An inclination of the device on the frontal plane would require the introdicion of another misalignment angle, β (magnified).

Chapter 4

Description of the calibration system

4.1 Introduction

A force platform (FP) is a complex, precision instrument. It requires accurate calibration, which is usually handled by the manufacturer prior to delivery. If the FP outputs are proportional to their respective inputs, the calibration process estimates the 6 proportionality coefficients. Unfortunately, this estimate is only approximately accurate since there is usually crosstalk between output variables. Due to the crosstalk, the six-by-six calibration matrix is not diagonal and includes non-zero, off-diagonal elements. Due to usage and age, the FP's sensitivity may change, and the manufacturer's calibration may become out-of-date leading to a lack of accuracy in the measurement of ground-reaction force and center of pressure (COP) [Chockalingam et al., 2002]. This may be harmful in movement analysis [Bobbert et al., 1991, ?] applications. In fact, these systematic errors may miscalculate:

- the location of the body center-of-mass, determined from ground-reaction forces [Lenzi et al., 2003];

- the estimation of energetic quantities, such as work or power [Meichtry et al., 2007];

- the estimation of joint forces and moments, determined from kinetic and kinematic data, through an inverse-dynamics approach [Cappozzo, 1984, Winter, 1991].

As an example, a COP mislocation of $\pm 1cm$ has been reported in literature [Schmiedmayer and Kastner, 2000] and is comparable to the manufacturer's specifications for most of the commercial FPs. This mislocation, during a gait analysis trial, produces errors comparable with the inter- [Harris and Smith, 1996] and intra- subject variability [Harris and Smith, 1996, Benedetti et al., 1998], and can also change the transition time between gait phases such as flexion and extension, as was exemplary shown in figure 2.2. A technique that minimizes the FP's systematic errors would be helpful to optimize the quality of the measured and estimated kinetic and energetic variables.

A new system that calibrates *in situ* a FP by the estimation of the six-by-six calibration matrix (**C**) of the FP wad designed and developed. Central to this system is an algorithm that estimates **C**. The system is composed also by a calibration device and a data-acquisition procedure.

The algorithm revises the one presented by Cappello et al. [2004], referred to as 2D-AL (thus 2-dimensional algorithm). In the 2D-AL, the inputs used to estimate $\mathbf{C}$ were time-varying 2-D loads, approximately aligned with the axes of the FP and perpendicular to the FP. The main differences in the two algorithms are: the revised algorithm requires 3-D, time-varying loads, and the loads have no alignment restriction.

4.2 Algorithm description

In the following, we consider the FP as the mechanical system combined with the calibration matrix provided by the manufacturer, and the FP output vector $\mathbf{L}$ as including three force and three moment components. The algorithm assumes a FP output vector explicitly including 3 force and 3 moment components. Anyway, different output vectors can be converted into the previous formalism, as shown in section 1.2.2.

The revised algorithm estimates the calibration matrix $\mathbf{C}$ starting from known loads $\mathbf{F}_I(t)$, imposed to the FP in a finite number of points, named hereinafter as "measurement sites", and the FP output vector $\mathbf{L}$. The $\mathbf{C}$ is a corrective operator that pre-multiplies the manufacturers calibration matrix. The FP deviation from ideality is represented solely by calibration errors and crosstalk phenomena. The input-output relationship can be described in the FP reference frame, by the equation:

$$\mathbf{L}_I = \mathbf{CL} + \mathbf{E} \tag{4.1}$$

where:

$$\mathbf{L} = \left[\begin{array}{c} F \\ M \end{array} \right] \qquad \text{six-component FP output vector;}$$

$$\mathbf{F} = \left[\begin{array}{c} F_X \\ F_Y \\ F_Z \end{array} \right] \qquad \text{force vector [N];}$$

$$\mathbf{M} = \left[\begin{array}{c} M_X \\ M_Y \\ M_Z \end{array} \right] \qquad \text{moment vector [Nm];}$$

$$\mathbf{L}_I = \left[\begin{array}{c} F_I \\ M_I \end{array} \right] \qquad \text{six-component input vector;}$$

$$\mathbf{C} \qquad \text{(6x6) calibration matrix;}$$

$$\mathbf{E} \qquad \text{Gaussian, uncorrelated, zero mean,} \\ \text{noise vector.}$$

$\mathbf{F}_I$ and $\mathbf{M}_I$ are related by the expression [Zatsiorsky, 2002]:

$$\left[\begin{array}{c} M_{XI} \\ M_{YI} \\ M_{ZI} \end{array} \right] = \left[\begin{array}{ccc} 0 & -Z_{COP} & Y_{COP} \\ -Z_{COP} & 0 & -X_{COP} \\ -Y_{COP} & X_{COP} & 0 \end{array} \right] \left[\begin{array}{c} F_{XI} \\ F_{YI} \\ F_{ZI} \end{array} \right] \qquad (4.2)$$

where X_{COP}, Y_{COP} and Z_{COP} are the coordinates of the COP in the FP reference frame (XYZ). The calibration principle can be summarized as follows:

1. the FP is loaded by known input loads;

2. $\mathbf{C}$ is calculated from equation 4.1, by a least-squares approach;

3. $\mathbf{L}$ is calibrated ($\mathbf{L}_C$) by equation 4.3.

$$\mathbf{L}_C = \mathbf{C}\mathbf{L} \qquad (4.3)$$

In a perfectly calibrated FP, $\mathbf{L}_C = \mathbf{L}$. Hence, the calibration matrix of a perfectly calibrated FP would be the six-by-six identity matrix.

The force $\mathbf{F}_I(t)$ can be calculated by an ideal triaxial load cell (LC), positioned on the FP surface at known measurement sites (k=1,...,n). The LC, figure 4.1, measures the force $\mathbf{F}_{LC}(t) = \begin{bmatrix} F_T(t) \\ F_L(t) \\ F_N(t) \end{bmatrix}$ its own right-handed, orthogonal reference frame (Transverse-Longitudinal-Normal, TLN), which is not necessarily parallel to XYZ. The rotation matrix ($\mathbf{R}^k$) between TLN and XYZ is not known *a priori*, and may be different for each measurement site. From equation 4.2 and for each $\mathbf{F}_{LC}{}^k(t)$, equation 4.1 can be written as:

$$\mathbf{P}^k\mathbf{R}^k\mathbf{F}_{LC}{}^k(t) = \mathbf{P}^k\mathbf{F}_I{}^k(t) = \mathbf{CL}^k(t) + \mathbf{E}^k(t) \qquad (4.4)$$

where $\mathbf{P}^k = \begin{bmatrix} 1 & 0 & 0 \\ 0 & 1 & 0 \\ 0 & 0 & 1 \\ 0 & -Z_{COP}{}^k & Y_{COP}{}^k \\ -Z_{COP}{}^k & 0 & -X_{COP}{}^k \\ -Y_{COP}{}^k & X_{COP}{}^k & 0 \end{bmatrix}$

Once all $\mathbf{R}^k$ are known, $\mathbf{C}$ can be calculated from equation 4.4 by a least-squares approach.

As a realistic assumption, the LC can be defined with the axis N parallel to the axis Z (Fig. 4.1). Therefore, each $\mathbf{R}^k$ reduces to a rotation about the Z axis and can be described by a single parameter α^k:

$$\mathbf{R}^k = \begin{bmatrix} cos(\alpha^k) & -sin(\alpha^k) & 0 \\ sin(\alpha^k) & cos(\alpha^k) & 0 \\ 0 & 0 & 1 \end{bmatrix} \qquad (4.5)$$

The revised algorithm estimates $\mathbf{C}$ from the following steps:

1. The misalignments, α^k, are initialized: $\boldsymbol{\alpha} = \begin{bmatrix} \alpha^1 \\ \dots \\ \alpha^n \end{bmatrix} = \mathbf{0}$;

2. The calibration matrix $\mathbf{C}$ is calculated by equation 4.4 by a least-squares approach;

3. The residual errors are estimated from equation 4.4 as:
$E^k(t) = \mathbf{P}^k\mathbf{R}^k\mathbf{F}_{LC}^k(t) - \mathbf{CL}^k(t)$;

4. The parameters update, $\Delta\boldsymbol{\alpha}$, is calculated by minimizing the cost function $\sum_{k,t} E^k(t)^T E^k(t)$, assuming dimensional unitary weights [Draper and Smith, 1966];

5. The parameters $\boldsymbol{\alpha}$ are updated: $\boldsymbol{\alpha} = \boldsymbol{\alpha} + \Delta\boldsymbol{\alpha}$.

The iteration of the steps $2 \div 5$ stops when each $\Delta\alpha^k < \varepsilon_0$, where $\varepsilon_0 = 10^{-10}$ is the chosen threshold.
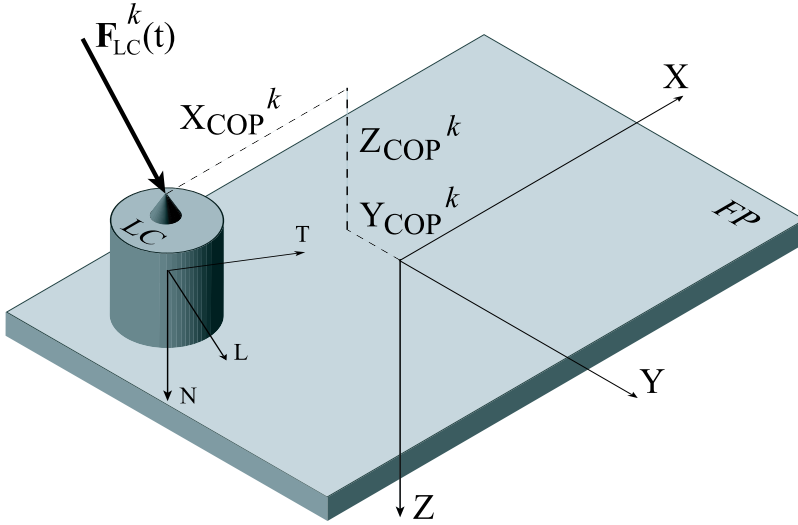
Figure 4.1: Schematic diagram of a force platform (FP) with a load cell (LC) on its surface. The time–varying force, $F_{LC}^k(t)$, is measured by the LC, and expressed in the LC reference frame (TLN). Simultaneously, the force is mechanically transmitted to the FP, and measured by the transducers of the FP, in its own reference frame (xyz). The known point of application of the force is expressed in the FP reference frame ($X_{COP}{}^k$, $Y_{COP}{}^k$, $Z_{COP}{}^k$).

4.3 Simulation tests

Common parameters for the simulation tests

The algorithm was analyzed through 4 simulation tests, in which a virtual FP with a known, true $\mathbf{C}$ was used. The algorithm had to estimate this $\mathbf{C}$, defined in equation 4.6.

$$\mathbf{C} = \begin{bmatrix} 1.0354 & -0.0053 & -0.0020 & -0.0287 & -0.0402 & 0.0081 \\ 0.0064 & 1.0309 & -0.0031 & 0.0210 & 0.0135 & -0.0001 \\ -0.0001 & -0.0004 & 1.0022 & -0.0005 & -0.0182 & 0.0300 \\ -0.0012 & -0.0385 & 0.0002 & 0.9328 & 0.0007 & 0.0017 \\ 0.0347 & 0.0003 & 0.0008 & -0.0002 & 0.9325 & -0.0024 \\ -0.0004 & -0.0012 & -0.0003 & -0.0023 & 0.0035 & 1.0599 \end{bmatrix} \quad (4.6)$$

The $\mathbf{C}$ used in all the 4 simulation tests propagates to the COP calculation introducing an error of about $1 \div 2$cm, similar as reported in literature [Schmiedmayer and Kastner, 2000]. Hence, the $\mathbf{C}$ defined in equation 4.6 can be considered as realistic.

Each test included 100 calibration runs. Each calibration run was initially simulated with a set of $n = 5$ measurement sites. The input loads relative to the 5 measurement sites were applied in the 5 COPs defined in equation 4.7

$$\begin{cases} X_{COP} &= (\quad 0, \quad 112, \quad 112, -112, -112)mm \\ Y_{COP} &= (\quad 0, \quad 192, -192, \quad 192, -192)mm \\ Z_{COP} &= (-124, -124, -124, -124, -124)mm \end{cases} \quad (4.7)$$

For each measurement site $k = 1, \ldots, 5$, $\mathbf{L}^k(t)$ was calculated from $\mathbf{F}_{LC}^k(t)$, with the following procedure:

- The signals $\mathbf{F}_{LC}{}^k(t) = \begin{bmatrix} F_T{}^k(t) & F_L{}^k(t) & F_N{}^k(t) \end{bmatrix}$ were generated as will be described in Section 4.3.1;

- The matrices $\mathbf{R}^k$ were generated using random rotations about the vertical axis in the range $\alpha^k = \pm 60°$;

- An uniformly distributed error in the range ± 1mm was superimposed onto the $X_{COP}{}^k$ and $Y_{COP}{}^k$ coordinates of the measurement site (LC placement error);

- The matrices $\mathbf{P}^k$ were defined using the coordinates of COP^k affected by error;

- A gaussian noise vector was added to $\mathbf{F}_{LC}{}^k(t)$. The noise had zero mean and standard deviations $\sigma_{LC} = \begin{bmatrix} 0.13N & 0.13N & 0.25N \end{bmatrix}$. The values of σ_{LC} were estimated by direct measurement on a custom LC (Laumas, Italy);

- $\mathbf{L}^k(t)$ was calculated from equation 4.4 with $\mathbf{E}^k(t) = 0$

- A gaussian noise vectors were added to the output signals. The noise had zero mean and standard deviation
$\sigma_{FP} = \begin{bmatrix} 0.49N & 0.49N & 0.72N & 0.15Nm & 0.11Nm & 0.12Nm \end{bmatrix}$. The values of σ_{FP} were estimated by direct measurement on a commercial FP (4060-08, Bertec Corporation, USA).

The LC was simulated as having a negligible non-linearity and hysteresis. Both LC and FP were supposed to work in stationary conditions.

The 95% confidence intervals (CI_{95}) of the generic parameter X (C_{ij} or α^k) was expressed as defined in equation 4.8 [Draper and Smith, 1966].

$$CI_{95}(X) = \sqrt{\Sigma_{XX}}\mathsf{t}(df, 1 - 0.025) \qquad (4.8)$$

where t is the Student's t-distribution, df is the number of degrees of freedom, and Σ_{XX} the parameter covariance matrix [Cappello et al., 2004]. The mean values of $CI_{95}(X)$, computed for the calibration matrix and the misalignment angles, were considered as indicators of the global precision of the respective estimates.

4.3.1   Optimal input signals

Methods

The revised algorithm was tested when using 3 different input waveforms, linear, oscillatory, and uniform, chosen for their different coverage of input force

domain. The first input, (figure 4.2, A) assumed a piecewise-linear variation for the components of with values defined in the range typical for walking tests at normal speed [Harris and Smith, 1996]. The second input (figure 4.2, B) was defined by two sinusoidal waveforms, shifted by 90°, for the horizontal forces, and by a ramp, for the vertical force. The third input spanned uniformly the 3D volume defined in the range:

$$\begin{bmatrix} -100 \div 100 & -100 \div 100 & 200 \div 600 \end{bmatrix} N \tag{4.9}$$

Each input waveform had 6000 samples.

The a priori identifiability of $\mathbf{C}$ was tested with no errors or noises added to the signals. Then, 100 calibration runs for each input waveform were simulated, using the FP and LC signals affected by noises and the COP positions of the measurement sites affected by errors (defined in Section 4.3).

Results

We found that $\mathbf{C}$ and the $\mathbf{R}^k$ were always *a priori* identifiable: the three input waveforms reported only numerical residuals ($< 10^{-10}$). In the 100 runs with the presence of noisy signals and COPs affected by errors, the revised algorithm estimated $\mathbf{C}$ with a precision equal to 1.09×10^{-3}, 0.91×10^{-3}, and 0.82×10^{-3} for the linear, oscillatory, and uniform input waveforms, respectively. Similarly, the revised algorithm estimated the α^k, with a precision equal to 0.16, 0.14 and 0.13 degrees.

Discussion

As resulted for the *a priori* identifiability tests, we verified the robustness of the revised algorithm in estimating the calibration and rotation matrices. These results did not depend on the specific input waveform. The three input waveforms were chosen to determine the sensitivity of the revised algorithm to different levels of richness in the information content of $\mathbf{F}_{LC}(t)$ (Fig. 4.2, B). The piecewise linear waveform was chosen as the simplest input, and the uniformly distributed waveform was chosen as the richest input, since it spans completely and uniformly the force domain of $\mathbf{F}_{LC}(t)$. The results of two such inputs can be assumed as estimates of the lower and upper bounds for the algorithm's performance. The oscillatory waveform (Fig. 4.2, B) was chosen as an intermediate level of richness, further this waveform can be approximately reproduced in practice.
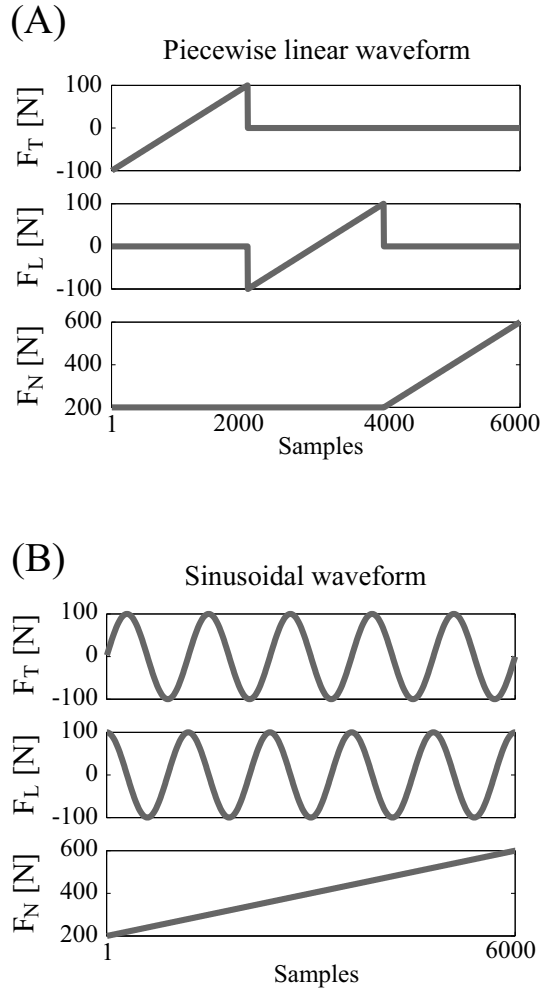
Figure 4.2: Examples of simulated input forces, $\mathbf{F}_{LC}{}^k(t)$, in the LC reference frame(TLN). Linear piecewise signals(A) and sinusoidal and cosinusoidal signals, for the horizontal forces, and linear signal for the vertical force (B).

4.3.2 Comparison with Cappello et al. [2004]

Methods

The revised algorithm was compared, in terms of accuracy and precision, with the 2D-AL algorithm. Both algorithms estimated $\mathbf{C}$ in 100 simulated runs. In each run, the COP-positions, errors, and noises were defined as in Section 4.3. The $\mathbf{F}_{LC}(t)$ for the revised algorithm was the 3-D sinusoidal waveform described above (Section 4.3.1). The $\mathbf{F}_{LC}(t)$ for 2D-AL was the same as the one used in that paper: similar to the sinusoidal waveform, but with one horizontal component of the load set to zero, hence laid in the TN or LN planes. The two algorithms were also compared in terms of the propagation of the error matrix $\Delta\mathbf{C}$ on the FP output signals, where $\Delta\mathbf{C}$ is the difference between the true 4.6 and the estimated $\mathbf{C}$. To this end, an input signal $\mathbf{L}_U(t)$ was used: the force components spanned completely and uniformly the 3-D force domain defined in the range 5.1; the moment components were calculated as defined in equation 4.2, using $\mathbf{L}_U(t)$ and the COP coordinates reported in 4.7. The maximum propagation error for each algorithm was quantified by the vector $\Delta\mathbf{L}$, with elements computed as:

$$\Delta\mathbf{L}_i = \max_t |\Delta C_i \mathbf{L}_U(t)| \tag{4.10}$$

where ΔC_i is the i-th row of the error matrix.

Results

For both algorithms, the mean values of the errors in the estimation of the calibration and rotation matrices was zero, hence the estimation process is unbiased in both cases. The CI_{95} obtained in the estimation of the calibration matrix by means of the algorithms, proposed in Cappello et al. [2004] and presented here, are shown in table 4.1. The proposed algorithm estimates the calibration matrix with a precision 5 times higher, on average, than the other. The maximum propagation errors of the 2 algorithms on the FP output signals are comparatively presented in figure 4.3. The new algorithm largely reduced the propagation of the matrix elements variability, mainly on signals F_X, F_Y, F_Z, and M_Z.

Discussion

This test proved that a 3-D input was advantageous to the algorithm performance, compared to a 2-D input. The propagation errors (Fig. 4.3) for F_X, F_Y, F_Z, and M_Z, were much higher with 2D-AL than with the revised algorithm. One possible explanation for this result is that the 2-D loads used in 2D-AL

Cappello et al. [2004]						Revised					
4.31	3.84	2.21	11.35	22.15	7.60	0.15	2.60	0.03	0.16	0.25	0.73
6.70	3.02	2.39	11.75	19.61	18.74	2.60	0.17	0.03	0.17	0.26	0.88
2.26	2.33	0.06	0.32	0.58	11.83	0.18	0.20	0.03	0.18	0.29	0.84
0.60	0.54	0.46	2.47	4.14	2.47	0.79	0.46	0.55	2.51	4.97	0.23
0.79	0.51	0.47	2.38	4.33	1.11	0.79	0.30	0.49	2.82	4.48	0.28
1.07	0.71	0.40	2.41	4.29	3.04	0.57	0.50	0.01	0.05	0.09	2.44

Table 4.1: 95% confidence intervals for the residual errors in the estimation of the calibration matrix. On the left, results obtained with the algorithm presented in Cappello et al. [2004], on the right, results obtained with the algorithm here proposed. All values are multiplied by 10^3
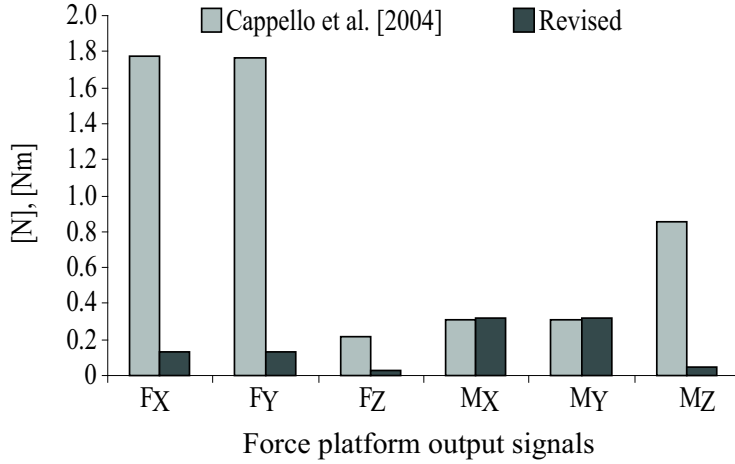
Figure 4.3: Maximum propagation errors of the calibration–matrix estimation on the FP output signals. The light–grey bars refer to the signals calibrated by the algorithm presented in Cappello et al. [2004]; the dark–grey bars refer to the signals calibrated by the new algorithm.

laid approximately in the XZ or YZ planes. As a consequence, the XY plane was scarcely investigated in the 2D-AL algorithm. Since M_Z is a function of F_X and F_Y, see equation 4.2, the omission of investigating the XY plane may have increased the errors in the M_Z calibration.

Finally, a comment on the small differences in the propagation errors of M_X and M_Y. This effect can be explained because M_X and M_Y are mostly influenced by F_Z (400 N on average) multiplied by Y_{COP} and X_{COP}, respectively, as shown in equation 4.2, with an error of about 1mm. As a consequence, an error in the COP may cause an error in the M_X and M_Y signals of about 0.4 Nm (as the one shown in Fig. 4.3).

4.3.3 Minimum number of measurement sites

Methods

The revised algorithm was tested with a number of the measurement sites between 1 and 9. The COPs used were the same five as defined in 4.7 and the 4 additional:

$$\begin{cases} X_{COP} &= (\ \ 224, \ \ 224, -224, -224)mm \\ X_{COP} &= (\ \ 384, -384, \ \ 384, -384)mm \\ Z_{COP} &= (-124, -124, -124, -124)mm \end{cases} \tag{4.11}$$

For each number of measurement sites, the revised algorithm estimated **C** of 100 simulated runs. In each run, the COP-positions, errors, and noises were as defined in Section 4.3.

Results

Figure 4.4 shows how well the revised algorithm estimated the calibration and rotation matrices and minimized the error-propagation, relatively to the number of measurement sites. As we had expected, the more measurements sites the revised algorithm used, the better results obtained. In particular, when using five or more measurement sites, the results were as precise as resulted in Section 4.3.1. When using less than 5 measurement sites, the precision of the algorithm exponentially decreased.

Discussion

The minimum number of measurement sites showed to be 5. We consider 5 measurement sites as a reasonable compromise between algorithm performance and system complexity.
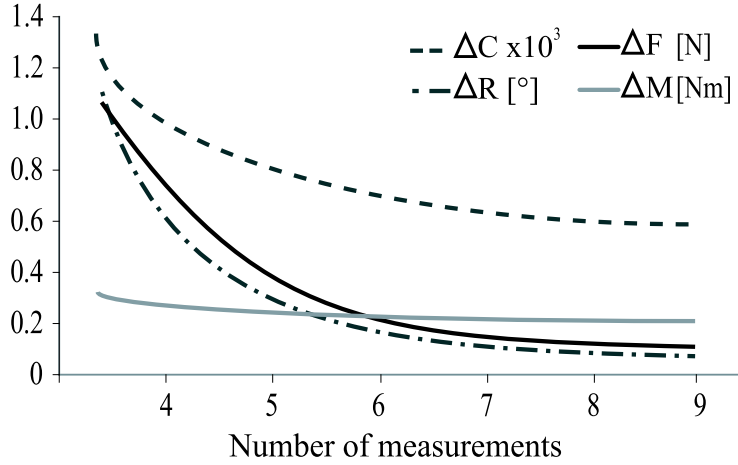
Figure 4.4: Performance of the revised algorithm while the number of measurement sites used in the estimation process is varied. The curves represent the global precision of the algorithm in the estimation of: the calibration matrix (dashed line); the rotation matrices, measured in degrees (dash-dot line); and the maximum error-propagation on the force platform output-signals, for the forces, measured in N (solid, black line) and for the moments, measured in Nm (solid grey line). For graphical purposes, the values relating to the calibration matrix are multiplied by 10^3.

4.3.4   Minimum distance between the measurement sites

Methods

The revised algorithm was tested when both X_{COP} and Y_{COP} coordinates, reported in 4.7, were multiplied by a scale factor ranging from 1 to 0.1, in steps of 0.001, in order to move closer the measurement sites. Consequently, the area covered by the measurement sites resulted reduced, ranging from $8.6dm^2$ to $0.9dm^2$. For each scale factor, the revised algorithm estimated $\mathbf{C}$ of one simulated run. For all the runs, the COP-positions, errors, and noises were as defined in Section 4.3.

Results

Fig. 4.5 shows the relationship between the performance of the algorithm when the distances between measurement sites was reduced. With a scale factor ranging from 1 to 0.5 (that correspond to a covered area greater than $2.7dm^2$), the performance of the algorithm did not change significantly; with a scale factor < 0.5 (covered area $< 0.5dm^2$), the algorithm performance exponentially decreased. For a covered area of $3.4dm^2$ the COP coordinates result:

$$\begin{cases} X_{COP} & = & (\quad 0, \quad 70, \quad 70, -\,70, -\,70)mm \\ Y_{COP} & = & (\quad 0, \quad 120, -120, \quad 120, -120)mm \\ Z_{COP} & = & (-124, -124, -124, -124, -124)mm \end{cases} \qquad (4.12)$$

Discussion

A reduction in the distance between measurement sites increased the bad conditioning of the $\mathbf{F}_{LC}{}^k(t)$ and, in turn, reduced the ability of the algorithm to estimate $\mathbf{C}$. Depending on what the calibration procedure will be used for and the specific use of the FP, different covered area could be chosen, with the limitation that the area must be $> 2.7dm^2$ (scale factor > 0.5).

Based on our simulation study, we would propose a calibration area of $3.4dm^2$ (scale factor of 0.625). With this value, more sets of 5 COPs can be located on a FP surface with the dimensions, for example, 400×600mm (4.6, sets labeled as II and III). Alternatively, another set (labeled as I) with a covered area greater of $13.44dm^2$ (scale factor of 1.25) can be chosen for the calibration procedure. The covered area of $3.4dm^2$ and $13.44dm^2$ provide, in respect of the whole FP surface, a reduced ("local") and an extended ("global") area for the calibration procedure. Local and global $\mathbf{C}$ could be helpful for example, when quantifying the non–linear behavior of a FP. In the simulated calibration–procedure, the FP was simulated without non–linearity; however, actual FPs can show non–linear effects [Schmiedmayer and Kastner, 1999]. Differences between local and global matrices may quantifying and compensating for the non–linearity in FP functioning.

4.4 Calibration device

The calibration device (Figure 4.7) consists of 3 major components: (1) a customized, triaxial LC, (2) an triangular stage, and (3) a mask.

The **load cell** is made of aluminium and steel (Laumas Elettronica, Italy).
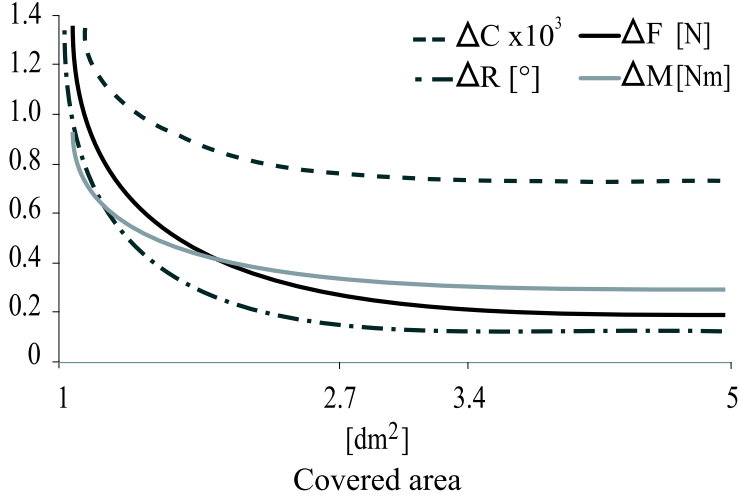
Figure 4.5: Performance of the algorithm while scaling the area covered by the measurement sites. The curves represent the global precision of the algorithm in estimating: the re-calibration matrix (dashed line); the rotation matrices, measured in degrees (dash-dot line); and maximum error-propagation on the force platform output-signals, for the forces, measured in N (solid, black line) and for the moments, measured in Nm (solid grey line). For graphical purposes, the values relating to the calibration matrix are multiplied by 10^3.

Technical specifications: full scale (FS) 500N shear forces and 1000N vertical forces; hysteresis 0.06%FS; non-linearity 0.05%FS. The LC works with 3 Wheatstone bridges, each one sensitive mainly to the force applied along the relevant axis of the LC reference frame, TLN. The LC was calibrated and certified by the metrological company Cermet (certificate number 0709020FRI). The LC calibration will be detailed described in the appendix. The LC was modeled with a quadratic model, as shown in equation 4.13:

$$F_i = A_i \begin{bmatrix} V_1 \\ V_2 \\ V_3 \end{bmatrix} + \begin{bmatrix} V_1 \\ V_2 \\ V_3 \end{bmatrix}^T B_i \begin{bmatrix} V_1 \\ V_2 \\ V_3 \end{bmatrix} \qquad (4.13)$$
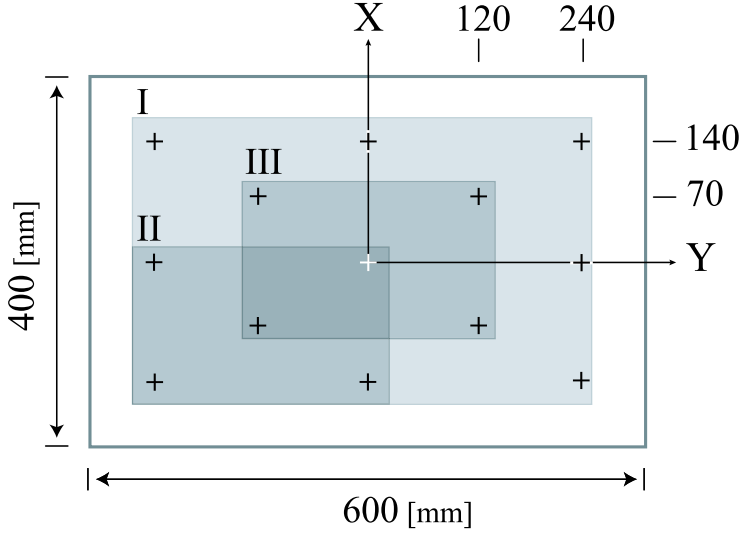
Figure 4.6: COP coordinates (+) for the chosen covered area ($3.4dm^2$). More sets (II and III) of at least 5 measurement sites can be identified on the FP surface. The set I results with a covered area greater than $3.4dm^2$. The sites are matched on a 600×400mm force platform.

where $i = T, L, N$ and $V = \begin{bmatrix} V_1 & V_2 & V_3 \end{bmatrix}^T$ is the LC voltage output. Vectors A_i (3×1) and matrices B_i (3×3) were estimated by a least-squares method from LC outputs and the applied loads. The LC has a circular base (ϕ=10cm) to reduce inaccuracies caused by FP deformation, due to a point source loading [Bobbert and Schamhardt, 1990, Middleton et al., 1999, Schmiedmayer and Kastner, 2000]. The top of the LC is a steel cone.

The LC bends when loaded, and the bending causes a variation in the COP coordinates. The maximal LC flexion was determined using a finite element simulation (Visual Nastran, MNC), in which the LC top was loaded with a horizontal force up to 200 N while the LC basement was fixed: the maximal COP variation resulted below 0.14mm, as shown in figure 4.8. This variation was considered negligible, based on results from a test in which the LC bending was included in a simulated calibration procedure.
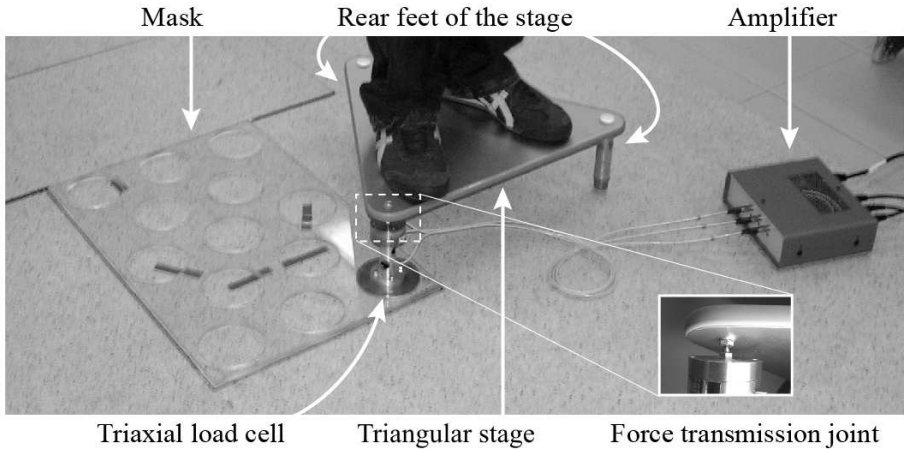
Figure 4.7: Calibration device.

The equilateral **triangular stage** is an aluminum base with a honeycomb structure that supports the subject. The dimensions of the stage are 600mm per side, and 16mm thick. Attached to two of the corners on underside of the stage are the rear feet, made of commercial-grade steel and brass. A ball bearing is attached to the bottom of two of the feet, to reduce ground friction. In the third corner of the stage there is a steel, conical socket that easily joins with the LC top. The vertex of the LC top is the only point of contact with the stage socket: the vertex coordinates constitutes the COP of the force applied to the LC. No torque is transmitted from the stage to the LC, hence the LC does not require to measure the torque. The mask is a 40×60cm sheet of plastic, placed during the data-acquisition procedure on the FP, and used to locate easily and precisely the LC on the FP.

The **mask**, made of plastic, used for the precise and easy placement of the LC on the FP surface. The mask has different sites (round holes with a diameter of 10cm), that result distributed on the whole FP surface. The site positions were determined by a simulation approach, as was described in section 4.3.4.

The voltage output of the LC was amplified by a customized charge am-
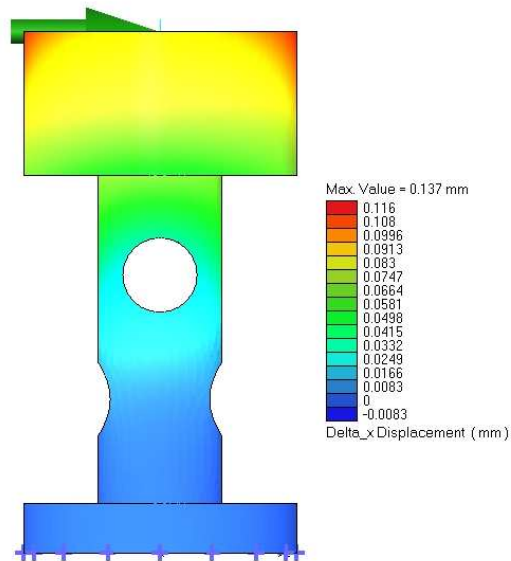
Figure 4.8: Bending of the load cell due to a horizontal force, F_X=200N. The bending was calculated by a finite elements simulation (Visual Nastran, MNC). The maximal horizontal displacement resulted 0.137 mm.

plifier, and the LC data were acquired using an acquisition board NI-DAQPad 6020E (National Instruments).The algorithm was implemented by the software **Matlab** (The Mathworks).

4.5 Data-acquisition procedure

The data-acquisition procedure is summarized as follows:

1. Both FP and LC electrical hardware were turned on, and a warm-up time was waited according to FP manufacturer's specifications;

2. The mask was manually positioned on the FP surface;

3. The LC was manually placed in one of the measurement site. The place-
   ment of the mask and of the LC caused a static offset of the FP output.
   Both FP and LC outputs were set to zero before proceeding, to eliminate
   the static offset;

4. The stage was placed as shown in Figure 4.7: the socket was placed on
   top of the LC, and the rear feet laid outside the FP surface;

5. A subject stood on the stage and swayed his body, generating a 3-D, time-
   varying load. In this way, the FP was loaded in its usual working range
   and did not require any external equipment to generate the load. Further,
   the stage resulted light-weight (2 kg), not cumbersome, and easy to move;

6. The LC and FP output were acquired for 30s, while the subject was sway-
   ing. The LC and FP acquisition systems were not synchronized, since
   working independently. The not-synchronized systems may introduce a
   time-synchronization error. This error is at worst half of the sampling fre-
   quency. By keeping a sampling frequency ≥1000Hz, such error is negligible
   (as resulted from a simulation test, described later);

7. Steps 3 ÷ 6 were repeated for all the measurement sites;

8. After data-acquisition, the LC and FP signals were synchronized via soft-
   ware, by finding the best cross-correlation between the vertical forces mea-
   sured by the LC and FP.

9. After synchronization, $\mathbf{C}$ was estimated by the algorithm, as described in
   section 4.2. The FP output vector $\mathbf{L}$ was calibrated ($\mathbf{L}_C$), as shown in
   equation 4.3.

The **minimum sampling frequency**, for an optimal calibration procedure,
was determined by a test.

Methods

In this test, a calibration procedure was simulated, as described in section 4.3.
Outcome of this simulation were the estimated variables $\mathbf{C}$, α and $\Delta\mathbf{L}$.

After this first estimation, the LC data were shifted of ±1ms and ±5ms, re-
spectively and the algorithm estimated again the variables, by using the original
FP data and the shifted LC data. The variables estimated with no time-shift
were subtracted to the variables estimated with a time-shift: the differences

	-5ms	-1ms	1ms	5ms
C $\times 100$	-0.26 ± 1.1	-0.04 ± 0.3	0.02 ± 0.4	0.09 ± 2.7
α [°]	-0.9 ± 0.9	0.1 ± 0.1	-0.2 ± 0.3	-1.8 ± 1.5
$\Delta\mathbf{L}$ [N, Nm]	1.3 ± 0.8	0.1 ± 0.3	0.4 ± 0.2	2.0 ± 1.1

Table 4.2: Results for the simulation test to determine the minimum sampling frequency. In table are reported the errors resulted while introducing a time-shift in the LC data. The numbers refer to the mean errors in the estimation of $\mathbf{C}$, α and $\Delta\mathbf{L}$.

were considered as an estimation of the non–synchronization error. The results are presented in table 4.2.

Results
The results are reported in table 4.2, for the time-shift of -5ms, -1ms, 1ms and 5ms respectively. The results are presented in terms of $\mathbf{C}$ estimation, $\mathbf{R}$ estimation (rotation angles α) and $\Delta\mathbf{L}$ calculation; the numbers refer to the average values and standard deviation.

Discussion
The error due to a time-shift of ± 1ms was considered as negligible, in fact, this error is comparable to the error resulted in the simulated calibration procedure, as described in section 4.3.

Chapter 5

Experimental validation of the system

Amti OR6
X_{COP}=(0, 70,   70, -70, -70,   0,   0, 140, -140, 194, 194, -194, -194)
Y_{COP}=(0, 120, -120, 120, -120, 240, 240,   0,   0, 172, -172, 172, -172)

Table 5.1: COP coordinates in [mm] used for the Amti force platform.

Common parameters for the experimental test

The new system was tested on 4 commercial FPs, three of which were strain-gauge FPs: Amti OR6 (size 46.4×50.8cm), Bertec 4060-08 (40×60cm), Bertec 4080-10 (40×80cm), and one was piezoelectric: Kistler 9286A (40×60cm).

These FPs are routinely used in clinical and research laboratories for gait and balance analysis. The FPs age was 5 ± 3 years. The X_{COP} and Y_{COP} of the measurement sites are defined in table 5.1 for the Amti FP, and in table 5.2 for the other FPs; for the FP Bertec 4080-10, 4 additional sites were used, in the COPs position defined in table 5.3.

We adapted the measurement sites position to the different FPs size, while keeping the reciprocal distance between the sites greater than the minimum distance, as defined in section 4.3.4, page 66.

In each measurement, the range of the input forces $\mathbf{F}_I(t)$ was defined in the range shown in equation 5.1. The same range experimentally measured was equal to the range used for the simulation tests, as described in section 4.3.1, page 60.

$$\begin{cases} F_T & \in & [-100 \div 100]N \\ F_L & \in & [-100 \div 100]N \\ F_N & \in & [200 \div 600]N \end{cases} \tag{5.1}$$

5.1   Linear calibration

Methods

For all the FPs, the algorithm estimated 5 local $\mathbf{C}$ using different subsets of 5 sites each: one subset referred to the FP center, as defined in table 5.4, and four to the FP corners, as exemplary defined in table 5.5.
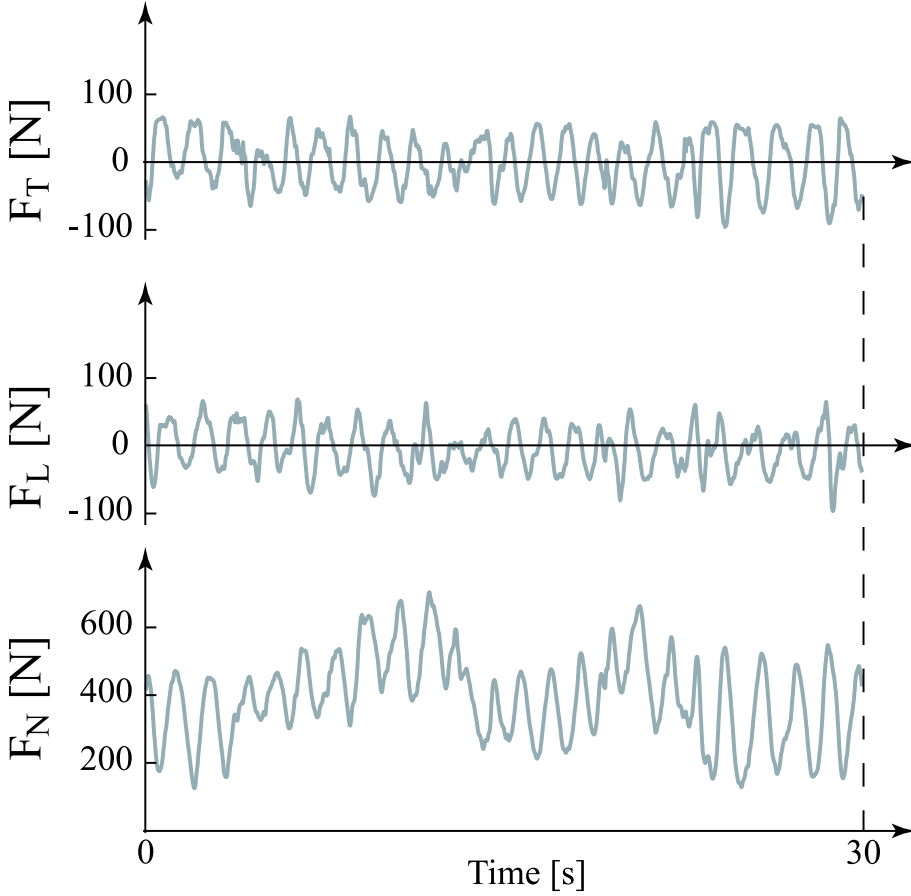
Figure 5.1: Typical force used with the calibration system, recorded during a measurement. The force is expressed in the load cell reference frame (TLN).

For all the FPs, the algorithm estimated one global $\mathbf{C}$, using all of the available measurement sites.

The difference matrices $\Delta\mathbf{C}$, were calculated as the difference between the estimated $\mathbf{C}$ and the six-by-six identity matrix $\mathbf{I}$, which was assumed to be the

Bertec 4060-80 , Kistler 9286A

X_{COP}=(0, 70,   70, -70, -70,   0,   0, 140, -140, 140, 140, -140, -140)

Y_{COP}=(0, 120, -120, 120, -120, 240, 240,   0,   0, 240, -240, 240, -240)

Table 5.2: COP coordinates in [mm] used for the Bertec and Kistler force platforms.

Bertec 4080-10

X_{COP}=(70,   70, -70, -70)

Y_{COP}=(340, -340, 340, -340)

Table 5.3: Additional 4 COP coordinates in [mm] used for Bertec 4080-10 force platform.

template of a perfectly calibrated FP ($\mathbf{L}_C$=$\mathbf{IL}$). The difference matrices $\Delta\mathbf{C}$ were considered the as an index of change in the FPs functioning. The effectiveness of the new system was verified by measuring the COP accuracy of the FP signals, pre- and post-calibration, when loading the FP in different, known COPs. For each local and global $\mathbf{C}$, we distributed the known COPs in the area delimited by the related subset of the measurement sites. The mean values of the COP signals, pre- and post-calibration, were subtracted from the actual COP values. The distance between the measured and actual COPs was considered a residual error.

Results

Central subset

X_{COP}=(0, 70,   70, -70, -70)

Y_{COP}=(0, 120, -120, 120, -120)

Table 5.4: Subset of COPs, in [mm], positioned in the center of the force platform.

Corner subsets

$X_{COP}=($	$0,\quad 70,\quad 0, 140, 140)$
$Y_{COP}=($	$0, 120, 240,\quad 0, 240)$
$X_{COP}=($	$70, -70,\quad 0,\quad 70, -70)$
$Y_{COP}=($	$340, 340, 240, 240, 240)$

Table 5.5: One of the subsets of COPs, in [mm], positioned near a corner, relatively to a 40×60cm and 40×80cm force platform.

Table 5.6 shows the percentage of the $\Delta\mathbf{C}$, regarding the global $\mathbf{C}$ and the standard deviation obtained from the five locals and the global $\mathbf{C}$ (numbers in brackets). The right column shows the average values of the $\Delta\mathbf{C}$, for the global calibration matrix and for the matrix variability (numbers in brackets).

The FPs Kistler and Bertec 4060 reported an average value for the global $\mathbf{C}$ <1%, while FPs Amti and Bertec 4080 reported an average value for the global $\mathbf{C}$ >1%; Kistler and Amti reported an average value for the $\mathbf{C}$ variability <1% while the two Bertec FPs reported an average value for the $\mathbf{C}$ variability >1%.

Table 5.7 shows the residual errors in the COP measurements pre-calibration and post- global and local calibration.

For the pre-calibration results, the average values of COP measurement errors for the Kistler and Bertec4060 FPs are <1cm, while for Amti and Bertec 4080, the errors are >1cm.

For the post-calibration results, the errors in COP measurements are smaller after a local calibration than after a global calibration. For all the FPs, the COP measurement errors are not homogeneously distributed on the FP surface, thus revealing a non–linear effect of the FP functioning. This result is exemplary shown in Figure 5.2 for the AMTI FP, where the errors are greater near the corners of the FP than in its center. Figure 5.2 shows also the residual errors in the COP measurement for the local calibration (grey area) than for the global, the results are consistent to table 5.7: the errors in COP measurements are smaller after local calibration than after global calibration.

		Kistler				Average
-0.5 (0.3)	-0.6 (0.3)	-0.1 (0.1)	0.3 (0.3)	0.6 (0.5)	-0.1 (1.5)	< 1 (< 1)
0.5 (0.3)	-0.9 (0.1)	-0.3 (0.0)	-0.5 (0.2)	-0.1 (0.4)	2.8 (1.3)	
-1.0 (1.5)	1.5 (0.8)	-1.5 (0.3)	-2.0 (1.1)	-4.3 (4.3)	-1.7 (7.4)	
-0.1 (0.3)	-2.5 (0.3)	0.0 (0.1)	-0.8 (0.3)	-1.3 (0.9)	-1.0 (1.8)	
2.8 (0.1)	-0.2 (0.1)	-0.1 (0.0)	-0.4 (0.3)	-0.8 (0.2)	0.1 (0.7)	
-0.5 (0.1)	0.2 (0.1)	0.0 (0.0)	0.1 (0.1)	0.0 (0.1)	-1.2 (0.3)	
		Bertec 4060				Average
-1.8 (1.7)	0.7 (1.4)	0.0 (0.7)	-0.5 (5.5)	-2.0 (1.6)	10.7 (14.7)	< 1 (> 1)
-0.4 (0.6)	1.0 (0.2)	-0.3 (0.1)	1.0 (0.7)	-0.8 (0.9)	-13.6 (7.7)	
-1.3 (0.9)	-1.3 (0.9)	-0.2 (0.5)	0.6 (4.2)	-0.5 (2.3)	3.5 (4.4)	
0.0 (0.1)	0.3 (0.2)	0.1 (0.1)	0.0 (1.0)	0.3 (0.2)	-1.4 (1.0)	
-0.4 (0.0)	0.1 (0.1)	-0.1 (0.0)	0.2 (0.3)	-1.3 (0.1)	-1.1 (0.6)	
-0.1 (0.2)	0.4 (0.2)	-0.1 (0.0)	-0.1 (0.3)	-0.5 (0.2)	0.8 (0.6)	
		Amti				Average
0.8 (0.4)	-1.7 (0.7)	0.4 (0.1)	0.8 (1.4)	1.7 (0.8)	8.4 (2.6)	> 1 (< 1)
2.9 (0.9)	3.0 (0.2)	-0.1 (0.1)	1.2 (0.7)	-1.0 (0.6)	-13.1 (3.0)	
1.3 (0.7)	-1.6 (0.7)	-0.2 (0.1)	-2.8 (1.0)	4.1 (1.4)	-1.4 (4.1)	
0.7 (0.1)	-4.0 (0.2)	-0.3 (0.0)	-6.0 (0.3)	0.3 (0.5)	-2.0 (1.6)	
5.3 (0.2)	-0.2 (0.1)	0.0 (0.0)	-0.5 (0.5)	-5.8 (0.4)	-4.3 (1.2)	
1.2 (0.2)	-0.9 (0.1)	-0.2 (0.1)	-0.1 (0.6)	-0.4 (0.5)	-1.9 (1.1)	
		Bertec 4080				Average
-18.9 (7.6)	3.2 (6.3)	4.3 (0.5)	0.1 (1.0)	-0.5 (1.1)	15.3 (57.8)	> 1 (> 1)
-6.6 (4.6)	-2.1 (1.9)	1.4 (0.4)	0.0 (1.3)	-0.5 (0.6)	-17.9 (22.7)	
-5.4 (1.2)	3.9 (3.7)	-2.5 (1.0)	-1.9 (4.7)	0.1 (1.0)	-7.3 (16.1)	
-1.3 (0.9)	0.6 (0.5)	1.1 (0.4)	-1.5 (1.4)	-1.1 (0.3)	-3.7 (2.7)	
0.1 (0.8)	-0.2 (0.3)	0.0 (0.2)	0.6 (0.5)	-3.3 (0.6)	1.2 (2.7)	
0.0 (1.2)	0.4 (0.8)	0.0 (0.1)	0.0 (0.8)	2.2 (0.2)	-1.4 (4.1)	

Table 5.6: Percentages of the difference matrices. Global calibration matrix and standard deviation resulting from local and global calibration matrices (numbers in brackets).

[*mm*]	Kistler	Bertec (4060)	Amti	Bertec (4080)	**Average**
pre	2.3 ± 1.4	2.6 ± 1.5	11.8 ± 4.3	14.0 ± 2.5	8.1 ± 6.0
post-					
global	1.1 ± 0.6	1.8 ± 1.1	1.0 ± 0.6	3.2 ± 1.1	1.9 ± 1.3
local	0.7 ± 0.4	0.8 ± 0.5	0.5 ± 0.3	2.0 ± 1.2	1.0 ± 0.9

Table 5.7: Residual errors in the COP measurement for the linear calibration, global and local, in comparison to the pre–calibration results.

Discussion

The $\Delta \mathbf{C}$ quantified the change in the sensitivity and crosstalk coefficients of the FPs. This change may be due to aging, usage and *in situ* installation of the FPs, and caused a lack of accuracy in the FPs data. The $\mathbf{C}$ estimated by the new system (table 5.6) compensated the lack of accuracy, as resulted in the increased COP accuracy, for all the tested FPs (table 5.7).

Local calibrations increased more the FP accuracy than global calibrations, this outcome was more effective for the Bertec 4060 and Bertec 4080 FPs. We considered 1% (Table 5.6, column of the average values) as a threshold to discriminate small or large lack-of-accuracy or non-linearity of the FP. In fact, regarding the lack-of-accuracy, with a value <1% (>1%), as reported in Table 5.6, correspond an error in the COP measurement <1cm (>1cm), as reported in Table 5.7; regarding the non-linearity, with a value <1% (>1%) the difference between local and global calibration is <1mm (>1mm).

Depending on the extent of the FP non–linearity, a local calibration would be preferable to a global calibration. A local calibration may compensate better the FP non–linearity since it calibrates the FP in a reduced area of the FP surface, and in a reduced area the extent of FP non–linearity could be reduced as well and could be better linearized by a calibration procedure.

An alternative to a linear calibration, when a FP show high non–linearity, can be the use of a non–linear calibration, as described in the next section.
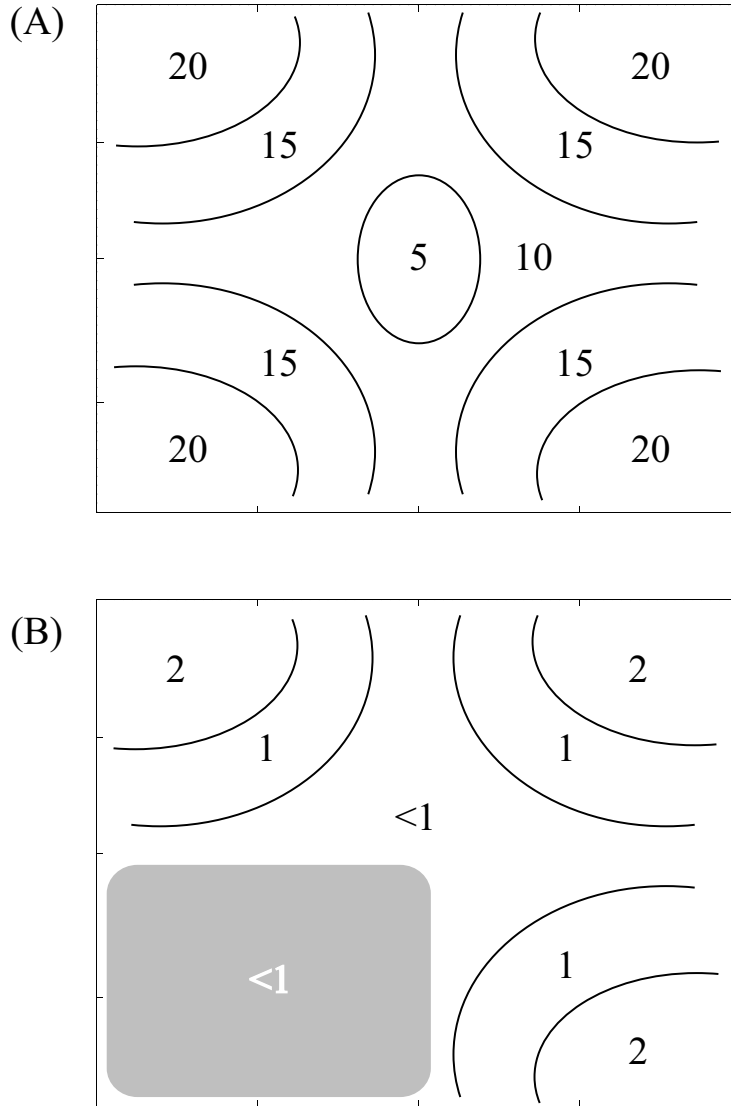
Figure 5.2: Accuracy in measurements of the center of pressure, pre-calibration (A) and post-calibration (B) for the Amti force platform. The numbers refer to the residual errors in mm. In (B), the black lines and numbers refer to global calibrations, while the grey area and the white number refer to one of the local calibrations.

5.2 Non–linear calibration

Introduction

In literature has been reported non–linear behavior of FPs [Mita et al., 1993, Schmiedmayer and Kastner, 2000]: deformation of the FP top plate due to load application, non–linearity of the load cells, and differences in characteristics among individual load cells, including amplifiers.

The presence of non–linearity is demonstrated also by the results obtained with the global and local calibrations: the better results obtained with local calibrations (reduced calibration area) showed that the mechanical functioning of the tested FP can only partially calibrated with a linear operator, the (6×6) calibration matrix.

Consequently, a non–linear calibration would be helpful in the compensation of the FP non–linearity.

The non–linear model proposed takes into account the top plate deformation: the deformation is principally due to the moment about the horizontal axes (as described in page 16).

Methods

The FP output vector ($\mathbf{L}$) is composed by the measured forces and moments and $\mathbf{L}$ can be calibrated ($\mathbf{L}_C$) using a non–linear calibration, as described in equation 5.2.

$$\mathbf{L}_C = \mathbf{C}\mathbf{L} +$$

$$+ \begin{bmatrix} C_{X\,11} & \cdots & C_{X\,16} \\ \vdots & \ddots & \vdots \\ C_{X\,61} & \cdots & C_{X\,66} \end{bmatrix} \begin{bmatrix} F_X \\ F_Y \\ F_Z \\ M_X \\ M_Y \\ M_Z \end{bmatrix} M_X + \begin{bmatrix} C_{Y\,11} & \cdots & C_{Y\,15} \\ \vdots & \ddots & \vdots \\ C_{Y\,61} & \cdots & C_{Y\,65} \end{bmatrix} \begin{bmatrix} F_X \\ F_Y \\ F_Z \\ M_Y \\ M_Z \end{bmatrix} M_Y =$$

$$= \mathbf{C}\mathbf{L} + \mathbf{C}_X\mathbf{L}_X + \mathbf{C}_Y\mathbf{L}_Y = \begin{bmatrix} \mathbf{C} & \mathbf{C}_X & \mathbf{C}_Y \end{bmatrix} \begin{bmatrix} \mathbf{L} \\ \mathbf{L}_X \\ \mathbf{L}_Y \end{bmatrix} = \mathbf{C}_{NL}\mathbf{L}_{NL}$$

$$(5.2)$$

where $\mathbf{C}_X$, $\mathbf{C}_Y$ and $\mathbf{C}_{NL}$ are respectively (6×6), (6×5), (6×17) matrices, and $\mathbf{L}_X$, $\mathbf{L}_Y$ and $\mathbf{L}_{NL}$ are respectively (6×1), (5×1), (17×1) vectors. The

differences between the equations 5.2 and 1.17 is the "incomplete" dimension of the $\mathbf{C}_Y$ and $\mathbf{L}_Y$: the element $M_X M_Y$ is missing, and consequently is missing also the fourth column of $\mathbf{C}_Y$, relative to the product $M_X M_Y$. If the element $M_X M_Y$, present in the matrix product $\mathbf{C}_Y \mathbf{L}_X$, were also present in the product $\mathbf{C}_X \mathbf{L}_Y$, the fourth–column elements of the matrices $\mathbf{C}_X$, $\mathbf{C}_Y$ would be not separately estimable hence, the estimation of such complete matrices would not be possible: the incomplete $\mathbf{C}_Y$ and $\mathbf{L}_Y$ must be used.

A practical advantage of this approach is that the non–linear calibration matrix can be estimated using the same data utilized for the linear calibration, hence, no additional measurements are required: the matrix $\mathbf{C}_{NL}$ was estimated for the same 4 FPs utilized for the linear calibration.

The estimation of $\mathbf{C}_{NL}$ was obtained with a two steps approach:

1. estimation of the linear, global matrix $\mathbf{C}$ and of the rotation matrices $\mathbf{R}$, the global $\mathbf{C}$ was calculated by using all the measurements performed on the FP;

2. estimation of $\mathbf{C}_{NL}$ utilizing all the measurements performed and the matrices $\mathbf{C}$ and $\mathbf{R}$ already estimated.

The first step is the estimation of the linear calibration matrix, as was described in section4.2.
The estimation of the non–linear calibration matrix can be summarized as follow:

α The matrix, $\mathbf{C}_{NL}$, is initialized as: $\mathbf{C}_{NL} = \begin{bmatrix} \mathbf{C} & \emptyset \end{bmatrix}$, where $\mathbf{C}$ is the (6×6) matrix estimated at the end of step 1 and $\emptyset$ is a (6×11) matrix of zero elements;

β For each measurement k an error function $(E^k(t))$ is calculated as follows: $E^k(t) = \mathbf{C}_{NL} \mathbf{L}_{NL}{}^k(t) - \mathbf{L}_I{}^k(t)$ where $\mathbf{L}_I{}^k(t)$ is the input vector, calculated with the matrices $\mathbf{R}^k$ estimated is step 1 and with $\mathbf{P}^k$ and $F_I^k(t)$ as defined in equation 4.4;

γ The matrix update, $\Delta\mathbf{C}_{NL}$, is calculated by minimizing the cost function $\sum_{k,t} E^k(t)^T E^k(t)$, assuming dimensional unitary weights [Draper and Smith, 1966];

δ Then the matrix is updated: $\mathbf{C}_{NL} = \mathbf{C}_{NL} + \Delta\mathbf{C}_{NL}$.

[*mm*]	Kistler	Bertec (4060)	Amti	Bertec (4080)
local linear	0.7 ± 0.4	0.8 ± 0.5	0.5 ± 0.3	2.0 ± 1.2
global non–lin.	0.7 ± 0.4	0.6 ± 0.2	0.5 ± 0.2	2.3 ± 1.3

Table 5.8: Residual errors in the COP measurement for the non–linear calibration, in comparison to the local, linear calibration.

The iteration of the steps β to δ stops when $\sum_{k,t} E^k(t)^T E^k(t) < \varepsilon_{NL}$, where $\varepsilon_{NL} = 10^{-8}$ is the chosen threshold.

A different approach was tried for the estimation: the estimation of both $\mathbf{C}_{NL}$ and $\mathbf{R}$ matrices. This approach would have the advantage to re-estimate the rotation matrices, thus to optimize the estimation of $\mathbf{R}$ for the non–linear calibration. This approach demonstrated to be unprecise in the contemporaneously estimation of those matrices.

Results
The results are presented in table 5.8, and report the residual error in the COP measurement; the results refers to the mean and standard deviation of the 5 linear, local calibration–matrices and to the non–linear calibration matrix. The residual errors of the local and linear calibrations are equivalent to the one obtained with the non–linear calibration.

Discussion
The non–linear calibration increased the FP accuracy as the local, linear calibration. The non–linear calibration, that was proposed in this thesis, can be considered as a valid method for the compensation of the non–linear effect of FP.

The proposed non–linear model takes into account the moment of the vertical force (about the horizontal axes), that can be considered to represent the flexion of the upper layer of the FP, as was described in chapter 1.2.2. The flexion was already pointed as possible cause of non–linearity in the FP functioning [Schmiedmayer and Kastner, 2000]; the proposed non–linear calibration compensated the non–linear effect, that was measured in the tested FPs. The proposed model can be considered as a experimental demonstration that the flexion of the FP upper layer is the main cause of the FP non–linearity.

A non–linear calibration can be applied as an alternative to a linear calibration, especially for the FP that show high non–linear effect. Both linear and non–linear calibration methods, shown in equation 4.3 and 5.2 respectively, can be introduced into a post-processing of the FP data, by a matricial multiplication: in this way, the FP data result calibrated without any intervention on the hardware structure.

5.3   Load range for an optimal calibration

The system described calibrated a force platform by means of input loads; the FP functioning therefore, results characterized in the same range: calibration therefore, is optimal for the particular range utilized.

In literature [Harris and Smith, 1996, Benedetti et al., 1998] is reported the range of the ground reaction force, typical for a gait task. The GRF, usually expressed in percentage of the bodyweight, would result, for a subject of 80 Kg (about 800 Newton):

$$\begin{cases} F_{ML} & \in & [-60 \div 60]N \\ F_{AP} & \in & [-180 \div 180]N \\ F_{VE} & \leq & 1000N \end{cases} \tag{5.3}$$

where F_{ML}, F_{AP} and F_{VE} are respectively the medio/lateral, antero/posterior and vertical force.

The range of the GRF, typical in quiet standing is much reduced than the range in gait tasks. Consequently, in order to have an appropriate calibration of a FP for gait or balance analysis, the range of the input loads used in the calibration process, should be the same as the range define for gait task: ± 180 N for the horizontal forces and up to 1000 N for the vertical force.

As previously described (page 77), the loads generated using the calibration system ranged ± 80 N for the horizontal forces and up to 600 N for the vertical force: this range is reduced, compared to the range used in gait analysis. The reduced range may influence the accuracy of the calibration process.

The system therefore was tested while varying the range of the input loads

Horizontal forces:	20	40	60	80	100	120	200	N
Vertical force:		400	450	500	550	600	650	1000	N

Table 5.9: Two sets of threshold used for the horizontal and vertical forces of the input loads.

used for the calibration matrix estimation.

An *ad hoc* calibration procedure was performed as previously described, on the FP Bertec 4060-80: in this procedure the horizontal forces ranged ± 200 N and the vertical force ranged up to 1000 N, 13 measurements were performed in the same COP positions as defined in table 5.2. Then, the algorithm estimated 7 matrices, while the value of a threshold was varied: the threshold was the upper limit for the horizontal forces, and the algorithm utilized only the measurement samples in which the horizontal forces were both below the fixed threshold. Finally, the same procedure was performed using a threshold for the vertical force and other 7 calibration matrices were estimated. For all the matrices estimated, both linear and non–linear algorithms were used.

The thresholds used for the two set of estimation are shown in table 5.9.

The accuracy of the calibration matrix was quantified by the COP accuracy of the FP. The signals used for the calibration process were also used for the COP accuracy estimation: the mean value of the COP, for each measurement, was subtracted to the actual COP value and the difference was considered as the residual error. For both sets of matrices, thus for the horizontal and the vertical threshold sets, the COP signals were calculated from the measurement signals in 2 different ways:

1. by using the samples below the corresponding threshold;

2. by using all the samples;

Results

Calibration resulted optimal for each horizontal or vertical threshold, when the COP was calculated by using the samples of the signals below the respective threshold.

Horizontal (shear) forces: 80 N

Vertical force: 550 N

Table 5.10: Minimum range of the input load for an optimal calibration, in regard of posture and gait analysis.

The calibration accuracy resulted to be dependent of the threshold, when the COP was calculated by using all the signal samples: this result is graphically shown in figure 5.3.

In regard of the horizontal forces threshold:

(A) the FP performance before calibration resulted not to be significantly dependent on the threshold used;

(B) the FP performance after a linear calibration resulted to be slightly dependent on the threshold used, the accuracy was comparable to the results presented in table 5.7 when using a threshold $\geq$80 N;

(C) the FP performance after a non–linear calibration resulted to be clearly dependent on the threshold used, also in this case, the results are comparable to the one presented in table 5.8 with a threshold $\geq$80 N.

In regard of the vertical force threshold, the results pre–calibration and post linear calibration reported no dependance to the threshold used, while

(D) the FP performance after a non–linear calibration resulted to be clearly dependent also on the vertical threshold used, the results are comparable to the one presented in table 5.8 with a threshold $\geq$550 N.

Discussion

The effectiveness of the algorithm, in the calibration matrix estimation, depends on the range of the input loads used in the estimation process.

Since in gait analysis the GRF range up to 200 N for the horizontal forces and up to 1000 for the vertical force, the system should optimize the FP functioning in this range of signals. Anyway, the system demonstrated to estimate optimally the calibration matrix using only a reduced range: by this range, the calibration matrix estimation showed to be optimal for signals with the same range typical in gait analysis, hence this range can be considered as the minimum range that should be used when calibrating a FP.
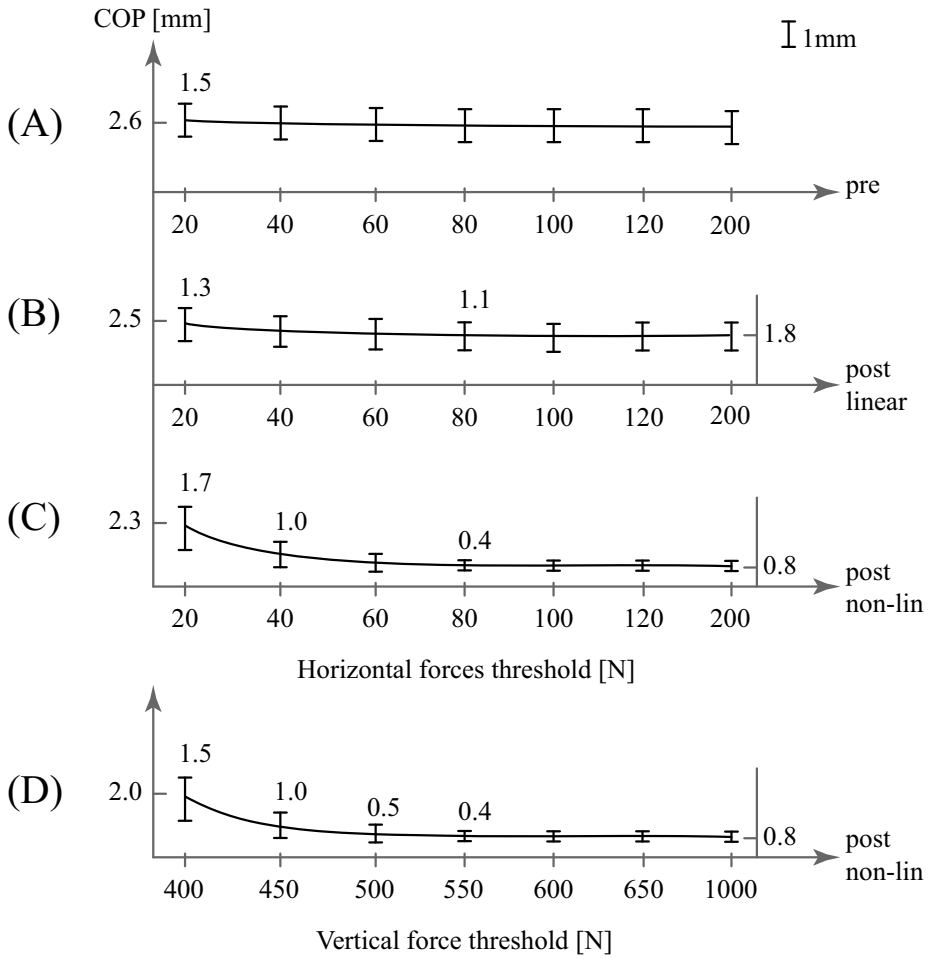
Figure 5.3: Influence of the range of the input signals on the system performance, quantified with the residual error in the COP measurement. (ABC) results for the threshold for the horizontal forces, pre–calibration and post- linear and non–linear calibration; (D) results for the vertical force threshold. The curve is the mean value and the vertical line is the standard deviation of the COP residual error.

Chapter 6

Influence of the FP calibration on inverse dynamics

6.1   Propagation on inverse dynamics

The purpose of this chapter is to answer the question:

"To which extent the force platform calibration influence the estimation of kinetic quantities, as the joint moments?"

This question is crucial, since it may justify the necessity of a periodical calibration of a FP.

Methods

To assess how the calibration process affects the estimates of kinetic quantities, such as joint net moments, a gait analysis test was performed on a subject from whom informed consent was first obtained. Measurement set-up included a Vicon 460 motion analysis system and the Bertec 4080-10 FP.

A set of 12 reflective markers, defined according to the Davis protocol [Davis et al., 1991], was used to measure the subject's kinematics. The subject was a young male, body weight 76 Kg, and height 1.86 m. The net joint moments were calculated on the sagittal plane, using a bottom-up inverse dynamics approach [Cappozzo, 1984] with adapted, inertial parameters [Zatsiorsky et al., 1990, de Leva, 1996]. The subject was modeled as a multilink with 3 joints (ankle-knee-hip). The centers of the ankle and knee joints were located at the midpoint between the lateral and medial malleoli and epicondyles, respectively. The center of the hip joint was calculated from the ASIS and PSIS makers, as described in [Shea et al., 1997]. Markers trajectories were filtered through a second-order, bidirectional Butterworth filter with a cut-off frequency set at 3 Hz [Cappello et al., 1996]. The net joint moments were calculated using the FP data pre- and post-calibration. The FP data were calibrated using the local **C** relative to the part of the FP loaded during the gait trial. The differences between the joint moments, pre-post calibration, were considered as an estimate of the propagation error due to the FP miscalibration.

Results

The results are shown in figure 6.1: the error due to the FP miscalibration is comparable to the intra–subject variability reported in literature [Benedetti et al., 1998]. It is noteworthy that, as a consequence of the calibration, the sign of the knee moment, as well as the transition time of hip moment from flexion to extension changed during the stance phase.

Discussion

As was already reported in literature, errors in the COP signals can propagate to the estimation of joint moments through inverse dynamics [Mc Caw and De Vita, 1995]. The result shown in figure 6.1 is hence consistent with literature.

Figure 6.1 clearly demonstrates that the FP calibration influences the estimation of kinetic quantities. A miscalibration in the FP data can be considered, therefore, as a possible source of error to be kept controlled in order to ensure a good quality for the gait analysis results. An appropriate calibration proved then as a necessary procedure that scientists and clinicians should adopt when using FPs.

The FP calibration influenced the calculation of the joint moments, which changed in terms of sign or transition-time between phases. This influence could be critical since the estimated joint moments are often the basis for clinical decision making, e.g. when planning a treatment or a surgical procedure in orthopedics.
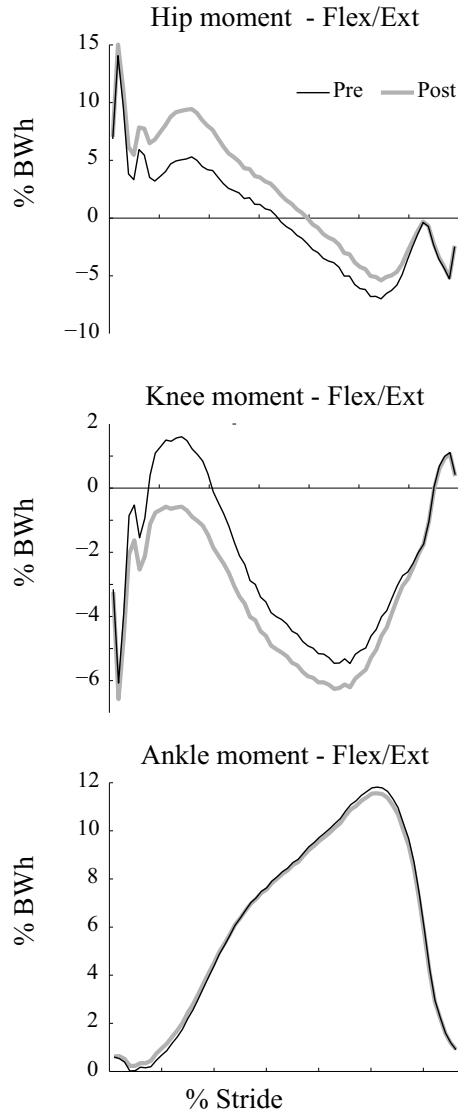
Figure 6.1: Propagation of the calibration to net joint–moment calculation. The results were obtained using a Bertec 4080-10 FP. The moments are expressed in percent, normalized to the subject body weight (BW) and height (h).

Chapter 7

Conclusions

This thesis focused on a novel portable system for the calibration of six-component force platforms. The system was designed to evaluate the accuracy of the FP in the working environment, where is routinely used (*in situ* calibration). The system was first presented from a theoretical point of view: the system design was described and the algorithm, core of the system, was described and optimized, by simulated calibration procedures. The requirements of the algorithm, for an optimal estimation of the calibration matrix, were analyzed in terms of: optimal input waveform, minimum number of measurements and minimum distance between the measurements. The algorithm gives the possibility to estimate local and global calibration matrices.

Second, an actual realization of the calibration system was presented and experimentally validated by testing the system on 4 commercial FPs. The calibrations performed showed that the system is effective in calibrating the FPs. Further, non–linear effects of the FPs were measured by the comparison between local and global calibration matrices. The residual errors in the COP measurement were comparable to the FP sensitivity threshold, as described in the FPs datasheet. We could conclude that the new system was effective in optimizing the FPs functioning. The FP non–linearity was compensated by a non–linear calibration methodology, proposed in this thesis. The minimum range of the input load, for an optimal calibration was defined by an experimental test.

Finally, the propagation of the calibration process on the estimation of net joint moments was quantified by a gait test, as described in the last chapter. The results clearly showed that the FP calibration can significantly influence the estimated kinetic quantities.

An effective and practical calibration procedure should be able to accurately calibrate the FP, and should be easily and quickly performed, in order to disturb the laboratory activity as less as possible. The novel system presented here satisfy all these requirements, thus can be considered as a possible solution routinely usable in laboratory and clinics for the HMA.

The results presented in this thesis provided a clear evidence of the need for a FP calibration in the field of HMA. Further, they suggest that any user should periodically calibrate the FPs, in order to maintain monitored their functioning status and to guarantee a high accuracy, for both FP data and estimated kinetic data. The over-time stability of a FP can be controlled for example by performing periodic calibration procedures (e.g. every 6 months). In that regards, a FP

could then be considered stable when the estimated calibration matrices differ by less than 1%. Differences in the estimated $\mathbf{C}$ larger than 1% may indicate that changes have occurred in the mechanics or electronics of the FP.

Appendices

Appendix A

Calibration of a 3D load cell

This appendix discuss how a load cell can be calibrated, by using different mathematical models. The models are firstly presented and secondly discussed, in terms of accuracy, by experimental results. The experimental results were obtained by the calibration of the triaxial load cell (LC) used in the calibration system described in this thesis. The LC was calibrated at the metrological company CERMET. The calibration was performed with particular attention to the non–linearity compensation.

The following sections describes

- the mathematical models used for the characterization of the triaxial LC;

- and the results obtained using the different mathematical models.

A.1   Mathematical models

The first model described regards a LC with one input and one output signal. For such LC, an example of the input/output relationship is shown in figure A.1. Let's consider that some measures (α, β and γ) were performed in order to calibrate the LC.

If the measurement points available were only α and γ, only a linear regression can be calculated, between the input x and output y, as shown in equation A.1.

$$y = mx + q \tag{A.1}$$

Anyway, a linear regression could not be enough precise if non–linearity is present, for example a second order non–linearity as shown in figure. In this case, the residual error would be almost zero for the points α and γ, but would be high for the points between α and γ. A more accurate linear regression can be achieved with additional measurement points (β): in this case, the regression can partially compensate the non–linearity and reduce the mean value of the residual errors. Formally, the regression equation is similar to A.1, but the coefficients can be different, in order to minimize the error.

A non–linear regression (second order in the figure) can be calculated only if additional measurement points are available (β). In this case, the input/output

relationship can be described as in equation A.2. A non–linear regression mini-mize the residual error better than a linear regression depending on the amount of non–linearity in the input/output behavior: the more non–linearity is present, the more a non–linear calibration results more effective.

$$y = ax^2 + bx + c \tag{A.2}$$
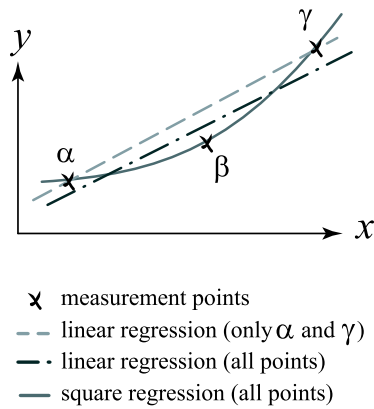
Figure A.1: Calibration models using linear and non–linear regression functions, for a 1-input/1-output relationship. Linear regression, using only the points α and γ (dashed), using all the points (dash-dot) and second order regression (solid).

In general, the use of n measurement points allows the estimation of a poly-nomial function with $n-1$ degree at maximum; if the degree is $< n-1$, the estimation would result more precise, since less parameter are estimated and consequently the error in the measurements results better compensated. A risk in a non–linear regression is the possible instability of the estimated function, for example when the measurement points are few compared to the order of the regression polynomial or not uniformly distributed in the measurement domain, or the measurement error is too high. These instability risks are exemplary shown in figure A.2. The estimation of a n-order polynomial, with less than $n-1$ points cannot give an unique solution and must be avoided; an estimation with a bad points distribution should be avoided as well, since small errors can cause huge inaccuracy in the estimation.
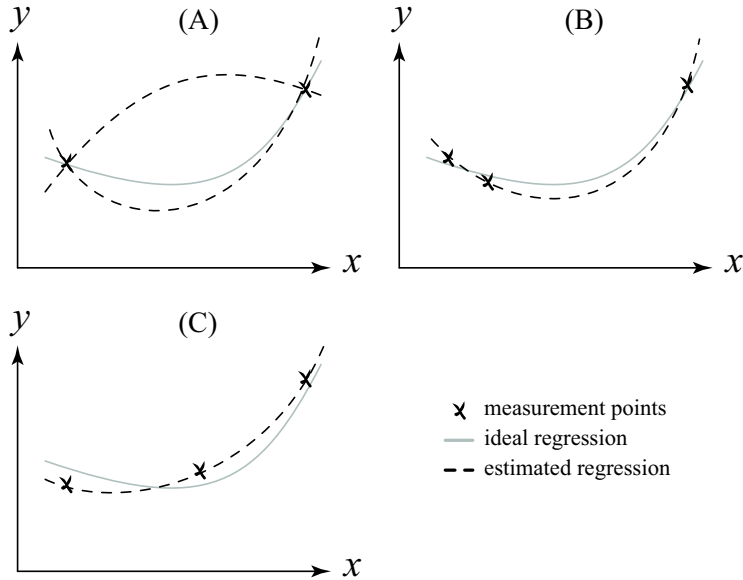
Figure A.2: Instability in a non–linear regression, caused by: (A) not enough points, compared to the order of the regression polynomial; (B) bad points distribution; (C) high measurement error.

The same approach can be applied if the output signal is function of more than one input signals. The input/output relationship must be calculated for all the input signals x_2 (i=1,... n), with a linear or a non–linear regression, as previously described. Each output signal requires a function $F_i(x_i)$ that can be linear or non–linear, depending on the input/output behavior between each input x_i and the output y.

In this case, the measurement points are taken only along the axes x_i and no points are measured inside the domain defined by the axes. Since no measurement points are presents, with more than one $x_i \neq 0$ contemporaneously, only a linear superimposition of the effects can be utilized, as shown in figure A.3 and in equation A.3.

$$y = F_1(x_1) + F_2(x_2) + F_3(x_3) \qquad \text{(A.3)}$$

Anyway, the linear superimposition of the effects could be only an approximation and non–linear crosstalk between the input variables may be present. In this case, as previously described for one input signal, a more accurate linear regression can be achieved with additional measurement points (β) internal to the measurement domain, as exemplary shown in figure A.3. The points internal the measurement domain allow a more accurate linear regression, that will correct the simple superimposition of the effects (equation A.3); alternatively, a non–linear crosstalk function can be estimated, in this case, equation A.3 should be modified as:

$$y = \sum_{i=1}^{3} F_i(x_i) + d_1 x_1 x_2 + d_2 x_2 x_3 + d_3 x_1 x_3 \qquad \text{(A.4)}$$

The parameters d_i quantify the non–linear crosstalk between the variables x_i, and represent the non–linear behavior of the points laying inside the measurement domain.

The models described can be used if more than one output signal is present. For each output signal y_i a different model and a different equation can be used, without the need to use the same model for all the outputs.

The LC used for the calibration system had 3 input and 3 output, y_1, y_2 and y_3: for each output signal an equation similar to A.4 was used.

A.2   Experimental measurements

Methods

The measurement points were obtained by following the measurement protocol proposed by the Cermet technical personnel; the protocol can be briefly described with the following steps:

1. positioning and blocking of the LC on a metal frame;

2. pre-loading of the LC by applying for a short time $F_N = 600N$, for the LC stabilization on the frame;
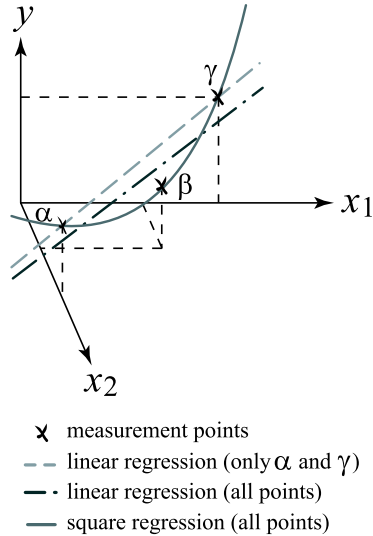
Figure A.3: Calibration models using linear and non–linear regression functions, for a 2-input/1-output relationship. Linear regression, using only points (α and γ) laying along the x_1 and x_2 axes (dashed line). Linear regression using also a point (β) internal to the measurement domain (dash-dot line). Second order regression (solid) using all the measurement points.

3. measurement of the zero signals for the 3 LC outputs with high precision voltmeters;

4. loading of the LC using high precision weights and measurements of the LC outputs;

5. unloading of the LC and measurement of the zero signals;

6. repeating of the two previous steps 3 times, for the repeatability calculation.

By the double measurement of the zero signal, a micro movement of the LC on the frame can be detected: when the LC is loaded, a mechanical stabilization can take place and cause the changing of the equilibrium condition of the LC.

This effect is revealed by the different zero signals measured (few mV). If a large difference in the zero signal was measured, the data acquired were discharged and the measurement process was repeated. By the LC pre-loading this effect rarely occurred.

In order to have a more precise estimation of the polynomial function, the measurement points taken were 13 for the horizontal axes and 9 for the vertical axis.

By the 3 times repetition of the LC loading, 3 sets of measurement were obtained and the percentage repeatability was calculated.

A set of measurement was repeated when, or the zero signals changed, or the repeatability error resulted high ($> 10\%$).

Different types of measurement were performed:

- mono-axial loading;

- multi-axial loading.

By the mono-axial loading, each LC axis (T,L and N) was loaded separately. This type of measurement consisted in the loading of the horizontal axis in the range (expressed in Newton):

$$F_T \ , \ F_L = (\quad 0, \quad \pm 10, \quad \pm 20, \quad \pm 40, \quad \pm 60, \quad \pm 80, \quad \pm 100) \text{N}$$

along the positive and negative directions, for a total of 13 measurement points.

The vertical axis was loaded in the following 9 points:

$$F_N = (\quad 0, \quad 100, \quad 200, \quad 300, \quad 400, \quad 450, \quad 500, \quad 550, \quad 600) \text{N}$$

By the multi-axial loading, the LC was positioned on an inclined frame (15°) and loaded, as shown in figure A.4. In this way, the load generated by the weights resulted decomposed along 2 or 3 axes: 2 axes (N and T or N and L) when the LC was rotated with an axis (T or L) laying in the plane defined by the vertical axis and the direction of the frame inclination; 3 axes when the LC was rotated of 45° in respect of the configuration previously described.

The same loading conditions used for the vertical axis were also applied here. In this configuration, the vertical load l resulted decomposed in $l \cos(15°)$ along the vertical axis and $l \sin(15°)$ along a direction orthogonal to the vertical. The

LC was aligned in 8 different positions (from 0° to 315° with a step of 45°).

The above described configuration was chosen because the LC is loaded in a similar way when used with the calibration system: the vertical load ranges around the weight of a human being and the shear forces range about ±100 Newton.

Three different LC calibration were estimated:

1. mono-axial linear calibration;

2. multi-axial linear calibration;

3. multi-axial square calibration.

For the mono-axial linear calibration, the linear regression coefficients were estimated, similarly as described in equation A.1 and in figure A.3 (dashed line). In the multi-axial, the regression coefficients were calculated using both mono and multi-axial measurement points; in this case the regression model was similar as in figure A.3, dash-dot line.

For the multi-axial square calibration, both mono and multi-axial measurement points were used for the estimation of the coefficients of square functions and crosstalk as defined in A.4, where F_i are quadratic functions, and i=T, L, N. The model used is similar to the solid line, shown in figure A.3.

The LC linearity error was calculated, after each of the 3 calibrations. The linearity error (LIN) is expressed for each LC axis as percentage of the ratio between the maximum error, in absolute value, between the measured (L_m) and the actual (L_a) load, and the full scale value (FS) of the corresponding axis (500N, 500N and 1000N respectively):

$$LIN = \frac{\max |L_m - L_a|}{FS} 100$$

Results

The results refer to the linearity error calculated for the 3 axes of the LC.

For the mono-axial, linear calibration:

a first linearity error (LIN_1) was calculated using only the mono-axial measurement points:

$$LIN_1 = [0.1\% \quad 0.06\% \quad 0.07\%]$$

a second linearity error (LIN_2) was calculated using all the measurement points:

$$LIN_2 = [1.2\% \quad 1.3\% \quad 0.3\%]$$

For the multi-axial, linear calibration, the linearity error (LIN_3) was calculated using all the measurement points:

$$LIN_3 = [0.5\% \quad 0.5\% \quad 0.1\%]$$

For the multi-axial square calibration, the linearity error (LIN_4) was calculated using all the measurement points:

$$LIN_4 = [0.3\% \quad 0.2\% \quad 0.1\%]$$

Discussion

A second order polynomial function was used for the LC calibration; the crosstalk behavior of the LC motivated this choice. Figure A.5 shows the voltage output corresponding to a horizontal axis, when the LC vertical axis was loaded (hence the crosstalk of the vertical on the horizontal axis): the behavior of the crosstalk is clearly non–linear and can be well described with a second order function.

The first result presented (LIN_1) shows a very high LC linearity anyway, the linearity error was calculated using only the mono-axial points (the axes of the LC force domain): this result is only partial, since the LC linearity was not verified for the points internal to the force domain (the multi-axial points).

In fact, if the LC linearity were calculated using both mono- and multi-axial points, the linearity error (LIN_2) results greater than LIN_1. These two results demonstrate that a mono-axial calibration may be not optimal when a non–linearity is present.

The third result (LIN_3) shows that the linear calibration performed with all the measurement points is more effective than the calibration performed with only the mono-axial points (LIN_2). A possible explanation of this effect can be the presence in the LC functioning of a non exact linear superimposition of the effects. The exploration of the points, internal to the LC force domain, allows a more precise estimation of the regression parameters. The parameters estimated may introduce variation to a pure superimposition of the effect, calculated using only mono-axial measurement points.

The last result (LIN_4) shows that the non–linear calibration of the LC was

more effective than the linear calibration, and remarks the presence of a non–linear behavior in the LC functioning.

As previously discussed, the calibration of the LC demonstrated to be about 2 times more accurate (second and third results) when performed with measurement points distributed along the axes and inside the force domain: the exploration of points inside the force domain seems to be necessary in the calibration of multi-axial transducers. Further, if non–linearity is present, a non–linear regression should be used.

Another advantage of the multi-axial measurement points is the higher repeatability of the measurements. Every measure is affected by instrumental error: when for example only one axis is loaded, the other two axes have a voltage output close to zero (only crosstalk is present), hence the instrumental error for these two axes results in percentage very high. On the other side, when all the 3 axes are loaded, all the 3 voltage output are $\neq 0$.
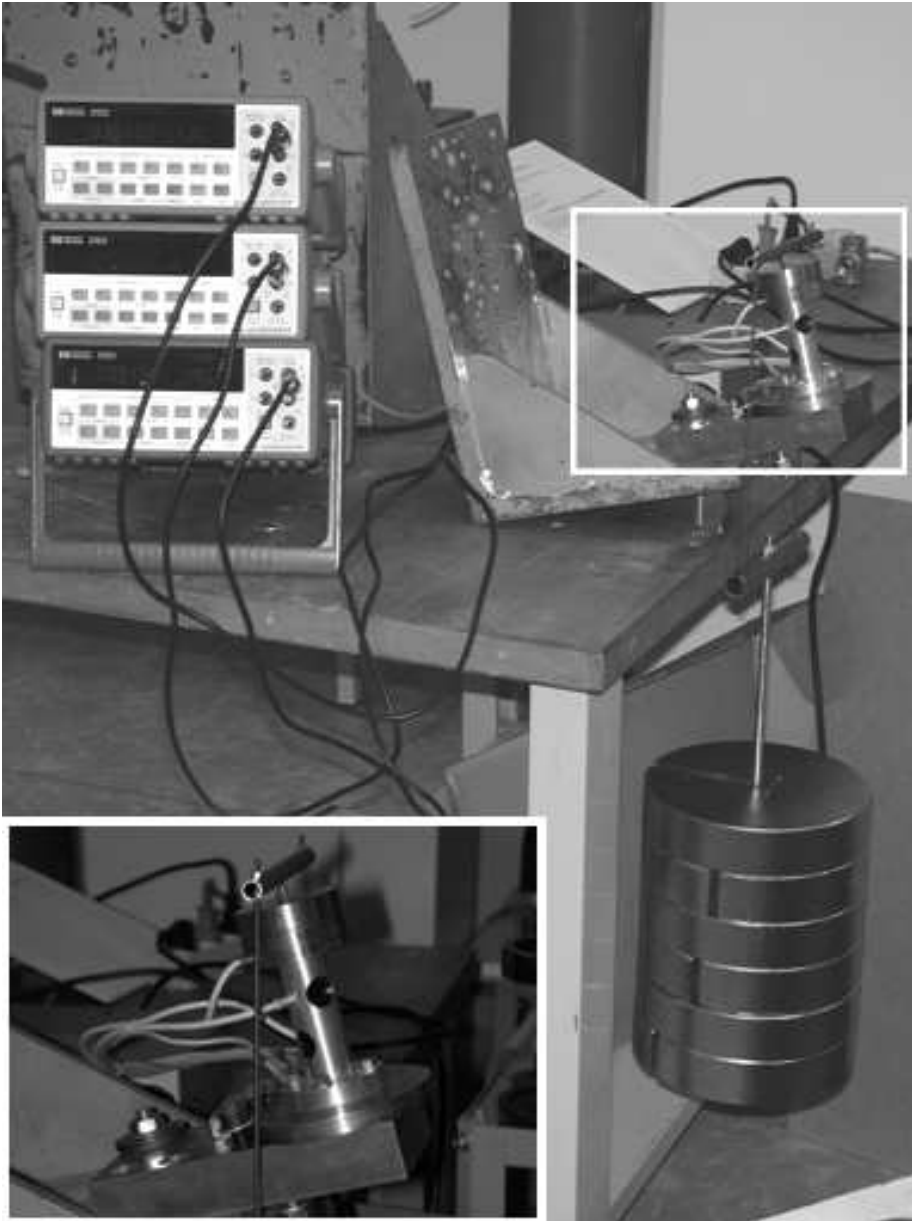
Figure A.4: Set-up for the load cell calibration. On the top left part of the figure, 3 precision voltmeters, on the bottom right part, 6 high precision weights used for the load cell loading. In the magnification, the load cell mounted on an inclined frame.
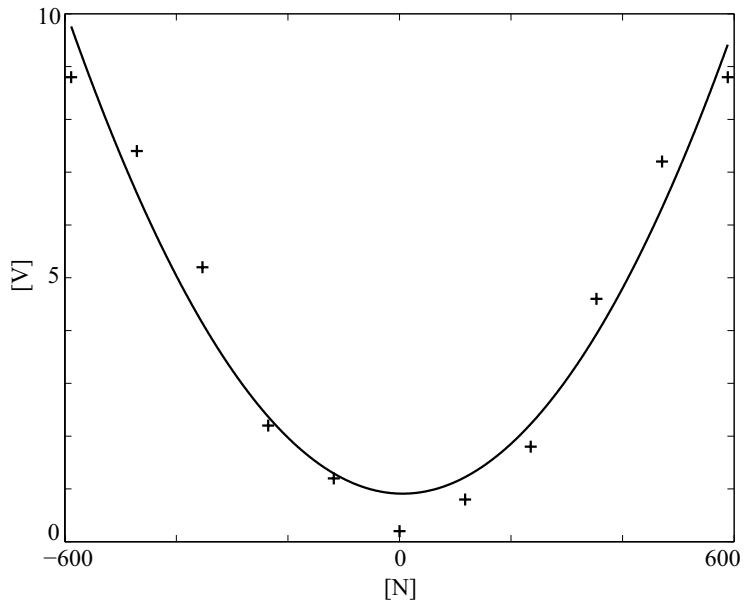
Figure A.5: Crosstalk of the load cell used for in the calibration system. The crosses are the experimental data in voltage. The figure shows the crosstalk between the vertical force (ranging from −600N to 600N) and the voltage output corresponding to one of the horizontal axes. The experimental data fits with a parabolic function, hence a square crosstalk was considered.

List of Figures

List of Tables

Bibliography

N Adamcova and F Hlavacka. Modification of human postural responses to soleus muscle vibration by rotation of visual scene. *Gait & Posture*, 25 (1): 99–105, 2007.

TP Andriacchi and AB Strickland. Gait analysis as a tool to assess joint kinetics. In N Berme, AE Engin, and KM Correira da Silva, editors, *Advanced Study Institute Biomechanics of Normal and Pathological Articulating Joints*, pages 83–102. Proceedings of NATO, 1983.

R Baker. The "poker" test: a spot check to confirm the accuracy of kinetic gait data. *Gait & Posture*, 5 (2):177–178, 1997.

R Baker. Gait analysis methods in rehabilitation. *Journal of NeuroEngineering and Rehabilitation*, 3 (4), 2006.

AL Bell, DR Petersen, and RA Brand. Prediction of hip joint centre location from external markers. *Human Movement Science*, 8:3–16, 1989.

MG Benedetti, F Catani, A Leardini, E Pignotti, and Giannini S. Data management in gait analysis for clinical applications. *Clinical Biornechanics*, 13 (3):204–215, 1998.

M Beppu, Y Ehara, S Monura, M Ikeda, and S Takahashi. Calibration of force plate with the method of least squares. *Bull. Kanagawa Prefectural Rehabil. Center*, 10:37–46, 1985.

N Berme and A Cappozzo. *Biomechanics of human movement, applications in rehabilitation, sports and ergonomics*. Washington, 1990.

Y Bing, ES Growney, FM Schultz, and KN An. Calibration of measured centre of pressure of a new stairway design for kinetic analysis of stair climbing. *Journal of Biomechanics*, 29 (12):1625–1628, 1996.

G Bizzo, N Guillet, A Patat, and PM Gagey. Specifications for building a vertical force platform designed for clinical stabilometry. *Medical and Biological Engineering and Computing*, 23:474–476, 1985.

MF Bobbert and HC Schamhardt. Accuracy of determining the point of force application with piezoelectric force plates. *Journal of Biomechanics*, 23:705–701, 1990.

MF Bobbert, HC Schamhardt, and BM Nigg. Calculation of vertical ground reaction force estimates during running from positional data. *Journal of Biomechanics*, 24(12):1095–1105, 1991.

RA Brand and RD Crowninshield. Comment on criteria for patient evaluation tools. *Journal of Biomechanics*, 14:655, 1981.

RE Brand. Can biomechanics contribute to clinical orthopaedic assessments. *Iowa Orthopaedic Journal*, 9:61–64, 1987.

J Browne and N O'Hare. A quality control procedure for force platform. *Physiological Measurements*, 21 (11):515–524, 2000.

A Burleigh, FB Horak, J Nutt, and J Frank. Levodopa reduces muscle tone and lower extremity tremor in parkinson's disease. *Canadian Journal of Neurological Sciences*, 22(4):280–285, 1995.

CAMARC II. Standards for instrumentation and specifications. In *Programme AIM, Technical report*, volume Project A-2002 C.E.C., August 1994.

N Capicíková, L Rocchi, F Hlavacka, L Chiari, and A Cappello. Human postural response to lower leg muscle vibration of different duration. *Physiological Research*, 55 (1):129–134, 2006.

A Cappello, PF LaPalombara, and A Leardini. Optimization and smoothing techniques in movement analysis. *International Journal of Bio-Medical Computing*, 41:137–151, 1996.

A Cappello, D Lenzi, and L Chiari. Periodical in-situ re-calibration of force platforms: a new method for the robust estimation of the calibration matrix. *Medical & Biological Engineering & Computing*, 42:350–355, 2004.

A Cappozzo. Gait analysis methodology. *Human Movement Science*, 2:27–50, 1984.

A Cappozzo, F Catani, A Leardini, MG Benedetti, and U Della Croce. Position and orientation in space of bones during movement: experimental artefacts. *Clinical Biomechanics (Bristol, Avon)*, 11(2):90–100, 1996.

N Chockalingam, G Giakas, and A Iossifidou. Do strain gauge force platforms need in situ correction? *Gait & Posture*, 16:233–237, 2002.

RD Crowninshield, RC Johnston, JG Andrews, and RA Brand. A biomechanical investigation of the human hip. *Journal of Biomechanics*, 11:75–85, 1978.

DM Cunningham and GW Brown. Two devices for measuring the forces acting on the human body during walking. *Proc Sot Expt Stress Analyt*, 9:75–90, 1952.

RB Davis, S Ounpuu, D Tyburski, and JR Gage. A gait data collection and reduction technique. *Human Movement Sciences*, 10:575–587, 1991.

P de Leva. Adjustments to zatsiorsky-seluyanov's segment inertia parameters. *Journal of Biomechanics*, 29:1223–1230, 1996.

PA De Luca. The use of gait analysis and dynamic emg in the assessment of the child with cerebral palsy. *Human Movement Science*, 10:543–554, 1991.

U Della Croce and P Bonato. A novel design for an instrumented stairway. *Journal of Biomechanics*, 40 (3):702–704, 2007.

HC Diener, J Dichgans, M Bacher, and B Gompf. Quantification of postural sway in normals and patients with cerebellar diseases. *Electroencephalography and clinical neurophysiology*, 57:134–142, 1984.

N Draper and H Smith. *Applied regression analysis*. John Wiley & Sons, Inc, 1966.

PS Fairburn, R Palmer, J Whybrow, S Fielden, and S Jones. A prototype system for testing force platform dynamic performances. *Gait & Posture*, 12:25–33, 2000.

GR Fernie and PJ Holliday. Postural sway in amputees and normal subjects. *Journal of Bone and Joint Surgery (American ed.)*, 60:895–898, 1978.

JR Gage. *Gait Analysis in Cerebral Palsy*. Mac Keith Press, 1991.

GM Galeazzi, D Monzani, C Gherpelli, R Covezzi, and GP Guaraldi. Posturographic stabilisation of healthy subjects exposed to full-length mirror image is inversely related to body-image preoccupations. *Neuroscience Letters*, 410 (1):71–75, 2006.

HS Gill and JJ O'Connor. A new testing rig for force platform calibration and accuracy tests. *Gait & Posture*, 5:228–232, 1997.

MM Gola. A calibration procedure of a new force plate. *Acta Orthopedica Belgica*, 46 (5):522–533, 1980a.

MM Gola. Mechanical design, constructional details and calibration of a new force plate. *Journal of Biomechanics*, 13:113–128, 1980b.

PA Goldie, TM Bach, and DM Evans. Force platform measures for evaluating postural control: reliability and validity. *Archives of physical medicine and rehabilitation*, 70:510–517, 1989.

ACH Guerts, B Nienhuis, and TW Mulder. Intrasubject variability of selected force-platform parameters in the quantification of postural control. *Archives of physical medicine and rehabilitation*, 74:1144–1150, 1993.

MG Hall, HE Fleming, MJ Dolan, SF Millbank, and JP Paul. Static in situ calibration of force plates. *Journal of Biomechanics*, 29-5:659–665, 1996.

GF Harris and PA Smith. *Human motion analysis*. IEEE press, 1996.

F Hlavacka and FB Horak. Somatosensory influence on postural response to galvanic vestibular stimulation. *Physiological Research*, 55 (1):121–127, 2006.

JP Holden, WS Selbie, and SJ Stanhope. A proposed test to support the clinical movement analysis laboratory accreditation process. *Gait & Posture*, 17 (3): 205–213, 2003.

A Hufschmidt, J Dichgans, KH Mauritz, and M Hufschmidt. Some methods and parameters of body sway quantification and their neurological applications. *Archiv für Psychiatrie und Nervenkrankheiten*, 228:135–150, 1980.

CR James, JA Herman, JS Dufek, and BT Bates. Number of trials necessary to achieve performance stability of selected ground reaction force variables during landing. *Journal of Sports Science and Medicine*, 6:126–134, 2007.

MP Kadaba, HK Ramakrishnan, and ME Wootten. Measurement of lower extremity kinematics during level walking. *Journal of Orthopaedic Research*, 8:383–391, 1990.

MP Kadaba, HK Ramakrishnan, ME Wootten, J Gainey, G Gorton, and GVB Cochran. Repeatability of kinematic, kinetic and electromyographic data in normal adult gait. *Journal of Orthopaedic Research*, 7 (6):849–860, 1989.

KH Kilburn, RH Warshaw, and B Hanson. Balance measured by head and a force platform in chemically exposed and referent subjects. *Occupational Environmental Med.*, 51:381–385, 1994.

CM Kim and JE Janice. Magnitude and pattern of 3d kinematic and kinetic gait profiles in persons with stroke: relationship to walking speed. *Gait & Posture*, 20:140–146, 2004.

RS Lakes, K Korttila, D Eltoft, A Derose, and M Ghoneim. Instrumented force platform for postural sway studies. *IEEE Trans. Biomechanical Engineering*, 28:725–729, 1981.

A Leardini, L Chiari, U Della Croce, and A Cappozzo. Human movement analysis using stereophotogrammetry. part 3. soft tissue artifact assessment and compensation. *Gait & Posture*, 21 (2):212–225, 2005.

D Lenzi, A Cappello, and L Chiari. Influence of body segment parameters and modelling assumptions on the estimate of center of mass trajectory. *Journal of Biomechanics*, 36:1334–1335, 2003.

A Lewis, C Stewart, N Postans, and J Trevelyan. Development of an instrumented pole test for use as a gait laboratory quality check. *Gait & Posture*, 26 (2):317–322, 2007. doi: doi:10.1016/j.gaitpost.2006.09.003.

V Litvinenkova and F Hlavacka. The visual feed-back gain influence upon the regulation of the upright posture in man. *Agressologie*, 14:95–99, 1973.

SD Lucy and KC Hayes. Postural sway profiles: Normal subjects and subjects with cerebellar ataxia. *Physiotherapy*, 37:140–148, 1985.

MR Mainenti, LF De Oliveira, MA De Melo Tavares De Lima, and J Nadal. Stabilometric signal analysis in tests with sound stimuli. *Experimental Brain Research*, 181 (2):229–236, 2007.

ST Mc Caw and P De Vita. Errors in alignment of center of pressure and foot coordinates affect predicted lower extremity torques. *Journal of Biomechanics*, 28:985–988, 1995.

A Meichtry, J Romkes, C Gobelet, R Brunner, and R Mueller. Criterion validity of 3d trunk accelerations to assess external work and power in able-bodied gait. *Gait & Posture*, 25:25–32, 2007.

J Middleton, P Sinclair, and R Patton. Accuracy of centre of pressure measurement using a piezoelectric force platform. *Clinical Biomechanics*, 14-5: 357–360, 1999.

K Mita, K Akataki, K Itoh, H Nogami, R Katoh, S Ninomi M Watakabe, and N Suzuki. An investigation of the accuracy in measuring the body centre of pressure in a standing posture with a force plate. *Frontiers of Medical and Biological Engineering*, 5-3:201–213, 1993.

PG Morasso, C Re, and M Casadio. Spotcheck and recalibration of stabilometric platforms. *Technology and Health Care*, 12:293–304, 2004.

M Murray, AA Seireg, and Sepic SB. Normal postural stability and steadiness: quantitative assessment. *Journal of Bone and Joint Surgery*, 57:510–516, 1975.

LF Oliveira, DM Simpson, and J Nadal. Calculation of area of stabilometric signals using principal component analysis. *Physiological Measurements*, 17: 305–312, 1996.

RJ Peterka and FO Black. Age-related changes in human posture control: sensory organization tests. *Journal of Vestibular Research*, 1(1):73–85, 1990.

K Pokorná. Use of stabilometric platform and visual feedback in rehabilitation of patients after the brain injury. *Prague Medical Report*, 107 (4):433–442, 2006.

TE Prieto, JB Myklebust, RG Hoffmann, EG Lovett, and BM Myklebust. Measures of postural steadiness: differences between healthy young and elderly adults. *IEEE Trans. Biomedical Engineering*, 43:956–966, 1996.

L Rocchi, L Chiari, and A Cappello. Feature selection of stabilometric parameters based on principal component analysis. *Medical and Biological Engineering and Computing*, 42:71–79, 2004.

L Rocchi, L Chiari, and FB Horak. Effects of deep brain stimulation and levodopa on postural sway in parkinson's disease. *Journal of Neurology, Neurosurgery & Psychiatry*, 73 (3):267–274, 2002.

L Rocchi, L Chiari, M Mancini, P Carlson-Kuhta, A Gross, and FB Horak. Step initiation in parkinson's disease: influence of initial stance conditions. *Neuroscience Letters*, 406(1-2):128–132, 2006.

HB Schmiedmayer and J Kastner. Parameters influencing the accuracy of the point of force application determined with piezoelectric force plates. *Journal of Biomechanics*, 32-11:1237–1242, 1999.

HB Schmiedmayer and J Kastner. Enhancements in the accuracy of the center of pressure (cop) determined with piezoelectric force plates are dependent on the load distribution. *Journal of Biomechanical Engineering*, 122:523–527, 2000.

KM Shea, MW Lenhoff, JC Otis, and SI Backus. Validation of a method for location of the hip joint centre. *Gait & Posture*, 5:157–158, 1997.

R Sommer, D Kohler, and C Calame. Center of pressure (cop) enhancement in piezoelectric force plates. In *Proceedings of the XVIth ISB Congress, Tokyo, p. 18*, 1997.

R Stagni, A Leardini, A Cappozzo, MG Benedetti, and A Cappello. E!ects of hip joint centre mislocation on gait analysis results. *Journal of Biomechanics*, 33:1479–1487, 2000.

C Stazio. *Hoho homini deus est, si suum officium sciat.* Number 265. Ribbek, 200 B.C.

CM Tylkowski, SR Simon, and JM Mansour. Internal rotation gait in spastic cerebral palsy in the hip. In *Proceedings of the 10th Open Scientific Meeting of the Hip Society*, Mosby, St.Louis, 1982.

S Uimonen, K Laitakari, R Bloigu, M Reinila, and M Sorri. Static posturography and intravenous alcohol. *Journal of Vestibular Research*, 4:277–283, 1994.

DA Winter. *Biomechanics and motor control of human gait.* University of Waterloo Press, 1991.

TF Winters, JR Gage, and R Hicks. Gait patterns in spastic hemiplegia in children and young adults. *Journal of Bone and Joint Surgery*, 69a:437–441, 1987.

V Zatsiorsky, V Seluyanov, and L Chugunova. *In vivo body segment inertial parameters determination using gamma scanner method.* In: N Berme and A Cappozzo. Biomechanics of Human movement, Applications in Rehabilitation, Sports and Ergonomics., 1990.

VM Zatsiorsky. *Kinetics of human motion.* Champaign IL, 2002.